Sister chromatid separation determines the proliferative characteristics upon whole-genome duplication through homologous chromosome rearrangement

Masaya Inoko[1], Guang Yang[1], Yuki Tsukada[2], and Ryota Uehara[1,3]

[1]Graduate School of Life Science, Hokkaido University, Japan

[2]Department of Biosciences and Informatics, Keio University, Japan

[3]Faculty of Advanced Life Science, Hokkaido University, Japan

Corresponding author:

Ryota Uehara, Faculty of Advanced Life Science, Hokkaido University, Kita 21, Nishi 11, Kita-Ku, Sapporo 001-0021, Japan

E-mail: ruehara@sci.hokudai.ac.jp

Phone: 81-11-706-9238

Summary

Whole-genome duplication (WGD) of diploid cells triggers various cell fates, such as cell death, cell cycle arrest, and proliferation with chromosome instability, contributing to broad bioprocesses, including differentiation, tumorigenesis, or aging. However, factors determining the post-WGD cell fates remain largely unknown. In this study, we found that cytokinesis failure (CF) and mitotic slippage (MS), two major routes of WGD induction, differentially affected post-WGD viability and proliferation in human cells. Quantitative live imaging revealed poorer survivability of cells upon multipolar chromosome segregation at the first mitosis after MS than CF. Chromosome-specific labeling showed that the lack of sister chromatid separation upon MS caused more skewed homologous chromosome distribution than CF. The skewed homologue distribution frequently led to physical isolation (> 10 μm) of the centrosomes from all homologous centromeres, hindering these centrosomes from capturing any of these homologues. The difference in the frequency of this nullisomic chromosome segregation between MS and CF well explained their difference in the viability of the subsequent daughter cells. Moreover, artificial separation of sister chromatids upon MS improved the evenness of homologue distribution, suppressed nullisomic homologue segregation in the following mitosis, and significantly restored the viability of their daughter cells. These results demonstrate the geometric arrangement of homologous chromosomes, defined by the presence or absence of sister chromatid separation upon WGD, as a key factor determining the proliferative characteristics of subsequent progenies. Our findings would provide a clue to understanding the route-dependent outcomes of WGD in cell fate determination in different bioprocesses.

Introduction

Whole-genome duplication (WGD) contributes to the progression of broad biological phenomena such as development, aging, cancer, and evolution (Conway et al., 2024; Darmasaputra et al., 2024; Van de Peer et al., 2017). Different cellular processes lead to WGD, causing various cellular outcomes, including cell death, differentiation, senescence, or proliferation with genome instability (Lau and Poon, 2023; Sanz-Gómez et al., 2023; Was et al., 2022). The complexity and diversity of causes and effects of WGD make it challenging to specify key factors affecting the characteristics of WGD cells. Nevertheless, identification of such factors is important for understanding the mechanisms of the different biological phenomena mentioned above.

Cell division failure is a critical cause of WGD in both physiological and pathological processes. There are two main types of cell division failure, cytokinesis failure (CF) and mitotic slippage (MS), leading to WGD (Was et al., 2022). CF occurs through defects in dividing the cytoplasm after normal chromosome segregation, forming a binucleated cell that contains two diploid nuclei. Besides spontaneous errors, physiological CF occurs in specific cell types in different tissues, such as hepatocytes, cardiomyocytes, or mammary epithelial cells (Hsu et al., 2016; Rios et al., 2016; Soonpaa et al., 1996). In case of hepatocytes, developmentally programmed suppression of cytokinesis factors mediates the progression of WGD (Hsu et al., 2016). Cancer cells also undergo frequent CF, which is explained, at least in part, by oncogene-mediated suppression of cytokinesis factors (Darp et al., 2022; Soeda et al., 2013).

MS is the premature exit from mitotic phase without chromosome segregation, forming a mononucleated cell that contains a single tetraploid nucleus (Was et al., 2022). Chromosome capturing by the spindle microtubules is a stochastic and error-prone process, and spontaneous defects in bipolar spindle formation cause a risk of chromosome segregation failure. Normally,

spindle defects result in the activation of spindle assembly checkpoint (SAC), which arrests mitotic progression until the defects are solved. However, suppression of SAC through loss-of-function of its components or attenuation of cdk1-dependent maintenance of the mitotic state lets cells escape mitotic arrest, leading to MS (Brito and Rieder, 2006; Haschka et al., 2018). Various cancer cells manifest altered expressions of SAC components, resulting in attenuated SAC function (Mondal et al., 2007; Schnerch et al., 2013; Sze et al., 2004; Wang et al., 2002). Similarly, cancer cells with low cdk1 activity show poor ability to undergo mitotic arrest, which is linked to their proneness to MS upon anticancer drug treatment (Sakurikar et al., 2012). Moreover, overexpression of v-Src oncogene induces MS by suppressing cdk1 activity (Horiuchi et al., 2018). In contrast to CF, physiological MS has been found in limited cases, such as megakaryocyte formation or DNA-damage-induced keratinocyte differentiation (Mazzi et al., 2018; Sanz-Gómez et al., 2020). Therefore, while CF and MS both result in WGD, their cellular causes, geometric features, and prevalence in biological contexts are different. However, it remains largely unknown whether CF and MS differentially affect post-WGD cell fates.

Several factors have been found to determine post-WGD cell fates. The p53 signaling pathway is the most studied mechanism, which is activated upon WGD and mediates cell cycle arrest, senescence, or apoptosis during interphase immediately after WGD (Aylon and Oren, 2011). Upon WGD, the centrosome number doubles, which induces inhibition or cleavage of Mdm2 to stabilize p53 through the activation of the Hippo signaling pathway or the PIDDosome multiprotein complex, respectively (Fava et al., 2017; Ganem et al., 2014). On the other hand, overexpression of cyclin D oncogene allows WGD cells to overcome the p53-mediated cell cycle arrest and proliferate (Crockford et al., 2017; Potapova et al., 2016). Moreover, proliferative post-WGD subclones established from p53-proficient diploid cell lines frequently manifest altered p53 signaling (Kuznetsova et al., 2015), possibly enabling them to override the WGD-linked anti-proliferative mechanisms.

Once cells evade cell cycle arrest or death immediately after WGD, they enter the first mitosis with 4 centrosomes. A part of these WGD cells cluster the excess centrosomes to form “pseudo-bipolar” spindles to conduct bipolar chromosome segregation (Ganem et al., 2009; Kwon et al., 2008; Silkworth et al., 2009). Moreover, the pseudo-bipolar spindle formation with asymmetric centrosome clustering (i.e., segregating in 1:3 ratio) contributes to efficient removal of the excess centrosomes in their progenies (Baudoin et al., 2020). Otherwise, WGD cells form multipolar spindles with the excess centrosomes, driving chromosome segregation into more than 2 daughter cells. Early studies by Boveri proposed that multipolar chromosome segregation occurs in a stochastic fashion, leading to drastic chromosome copy number alterations (Boveri, 1914). A substantial proportion of such multipolar daughters are supposed to die due to their lethal karyotypes. On the other hand, the remaining survivors potentially contribute to clonal evolution of WGD progenies with gross aneuploidy, hence driving phenotypic diversification (Gisselsson et al., 2008; Gisselsson et al., 2010; Yang et al., 2012). Indeed, a frequent multipolar cell division results in the formation of aneuploid progenies after physiological WGD in hepatocytes (Duncan et al., 2012). Therefore, the quality of multipolar chromosome segregation in the early post-WGD phase can be one of the critical factors determining the characteristics of post-WGD cell populations. Importantly, most of the above-mentioned post-WGD alterations (i.e., the excess centrosome gaining, p53 signaling, or multipolar spindle defects) occur in common either after CF or MS (Fava et al., 2017; Potapova et al., 2016), having drawn no attention to possible impacts of differences in the route of WGD induction.

In this study, we systematically compared post-WGD cell proliferation after MS or CF using HCT116, a near-diploid human cell line commonly used in ploidy comparative studies (Bernhard et al., 2023). Through a quantitative live imaging analysis, we found that MS-derived WGD cells manifested poorer survivability through the first mitosis than CF-derived ones, particularly when

undergoing tripolar chromosome segregation. Homologous chromosome labeling analyses revealed that MS-derived WGD cells more often formed nullisomic daughters upon multipolar chromosome segregation than CF-derived ones, which quantitatively explained the above difference in viability of post-WGD progenies between MS and CF conditions. By tracing the dynamics of homologous chromosomes in the first mitosis after WGD, we specified that the MS-linked increase in nullisomic chromosome segregation occurred due to a more skewed distribution of homologous chromosome territories after MS than CF. Artificial induction of precocious sister chromatid separation upon MS significantly improved evenness of homologous chromosome territories, reduced nullisomic chromosome segregation, and increased viability of daughter cells. Our findings demonstrate that the geometric profile of intranuclear organization of acute WGD cells, determined by transient cellular events upon WGD, has a crucial long-term influence on the proliferative characteristics of post-WGD progenies.

Results

MS-derived WGD cells are less proliferative than CF-derived ones

To gain insight into potential differences in properties of WGD cells derived from different types of cell division defects, we compared cell proliferation following pharmacological induction of MS or CF in near-diploid colorectal cancer cells, HCT116. MS-derived WGD (MS-WGD, hereafter) was induced by arresting cells at prometaphase by nocodazole shake-off, and subsequently forcing them to undergo mitotic exit without spindle formation by co-treating nocodazole and a cdk1 inhibitor RO3306 (see Materials and methods for details) (Fig. 1A). CF-derived WGD (CF-WGD) was induced by removing nocodazole from the above prometaphase-arrested cells, and subsequently treating with cytochalasin B (Fig. 1A). These compounds were thoroughly washed out after 2-h treatment. Efficiency of MS- or CF-WGD induction, assessed by possession of the excess centrosomes, was 85% or 82%, respectively (Fig. 1B, S1A and B). As expected, most MS- or CF-WGD cells had a single nucleus or two nuclei, respectively (Fig. 1B and S1C).

These WGD-induced cells were seeded at 2,000 cells/well in a 6-well culture dish. Cells forming colonies after 8- or 9-d culture were stained with Hoechst33342 for quantifying DNA content distributions in individual colonies using fluorescence microscopy (Fig. 1A, C, and D). Histogram of DNA contents in most colonies showed typical cell cycle distributions consisting of G1 and G2/M peaks, indicating the proliferative state of these cell populations (Fig. 1D and Supplemental material S1). Ploidy levels estimated from the relative G1 DNA contents of individual subclones distributed in a bimodal fashion, peaking at either near-diploid or polyploid (> 3 C) (Fig. 1E). For the following reason, these near-diploid subclones were likely originated from the cells that escaped WGD induction: Based on the WGD induction rates (Fig. S1B), about 50-300 out of 2,000 cells were assumed to remain in the diploid state (i.e., escaping WGD induction) when seeded after

WGD induction. When equivalent numbers of untreated diploids were seeded, we obtained numbers of diploid colonies that roughly corresponded to those obtained after the aforementioned WGD induction (Fig. S1D). Therefore, we excluded these near-diploid colonies and quantified the number of polyploid colonies to assess the proliferation ability of the post-WGD cells (Fig. 1F). We found that CF-WGD cells reproducibly formed significantly more polyploid colonies compared to MS-WGD cells (Fig. 1F). Therefore, MS-WGD cells had poorer proliferative ability than CF-WGD, indicating different impacts of these two routes of WGD on subsequent cell proliferation. Since this "context-dependent" difference in post-WGD cell proliferation was novel, we decided to address the cellular processes differentially affected between MS- and CF-WGD cells.

Poorer survivability of MS-WGD cells through multipolar chromosome segregation at the first mitosis

The significantly lower number of colonies formed after MS-WGD than CF-WGD indicates that earlier processes of cell proliferation were more severely compromised in the former case. We addressed this possibility by live imaging in HCT116 cells expressing histone H2B-mCherry as a chromosome marker to investigate the progression and fates of the first mitosis after MS- or CF-WGD (Fig. 2A and B). A substantial proportion of cells entered mitosis after MS- or CF-WGD induction (81% or 80%, respectively), while the remaining stayed or died in interphase (Fig. S2A). Diploids that escaped WGD induction were distinguished from WGD cells based on either nuclear area immediately before mitotic entry and excluded from the analyses (Fig. S2B). Because of the excess centrosomes gained upon WGD, either MS- or CF-WGD cells suffered an equivalently high frequency of multipolar chromosome segregation (89% and 86%, respectively; Fig. 2B, C, and S2C). Mitotic duration was not significantly different between MS- and CF-WGD cells (measured from nuclear envelope breakdown, NEBD, to mitotic exit; 40 min and 34 min, respectively) (Fig. S2D).

Multipolar chromosome segregation caused variation in DNA content in the resulting daughter cells (F1 cells, hereafter). We found that, at each mitotic event, the nuclear H2B-mCherry signal was segregated into F1 daughters at the ratio that recapitulated those measured by Hoechst33342 (Fig. S2E and F). Therefore, assuming that P0 cells had 8C DNA content at the first mitosis after WGD, we estimated the DNA content of each F1 cell using the H2B-mCherry segregation ratio (Fig. 2D). We noticed that a substantial proportion of F1 cells fused and became multinucleated (Fig. 2B, S2C, and S2G). Therefore, we separately analyzed these fused F1 populations from the unfused ones. Reflecting the stochastic nature of multipolar division, DNA contents were heterogeneous among individual F1 cells (Fig. 2E). DNA contents in unfused F1 cells from bipolar, tripolar, or tetrapolar chromosome segregation were on average 4.0, 2.7, or 2.1 C, respectively, both in MS- and CF-WGD (Fig. 2E). DNA contents in F1 cells fused after tripolar or tetrapolar chromosome segregation were on average >5.0, or 3.9 C, both in MS- and CF-WGD (Fig. 2E). Therefore, either reduction in the polarity of chromosome segregation or daughter cell fusion contributed to increasing DNA contents in F1 cells.

Next, we analyzed fates of F1 cells, which were categorized as “divided” (entered the subsequent mitosis), “arrested” (stayed alive without cell division for more than 36 h), or “died” (underwent cell death during the F1 cell cycle; Fig. 2E, S2H, and I). MS-WGD cells produced significantly fewer “divided” F1 progenies than CF-WGD cells (Fig. S2I). We also compared F1 cell fates sorted by their DNA contents, polarity of chromosome segregation, or the presence or absence of fusion (Fig. 2F, G and S2J). CF-WGD F1 cells gained a significantly higher chance of viability (judged by the frequency of “divided” cells) when they obtained higher DNA contents (Fig. 2F). Consistent with this trend, either the reduction in chromosome segregation polarity or daughter cell fusion resulted in higher F1 cell viability (Fig. 2G and S2J). Whereas the viability of MS-WGD F1 cells also increased with higher DNA contents, that with 1.5-3.5 C DNA contents was significantly lower

in MS-WGD than in CF-WGD (Fig. 2F). Similarly, the viability of tripolar chromosome segregation-derived MS-WGD F1 cells was significantly lower than that of CF-WGD F1 cells (Fig. 2G). This result indicates that cells are less tolerant to a reduction in DNA content through multipolar chromosome segregation in the MS-WGD condition than in the CF-WGD condition.

Non-random chromosome segregation causes frequent nullisomy after MS-WGD

We next addressed the reason for the poorer viability of MS-WGD cells than CF-WGD cells after multipolar chromosome segregation at the first mitosis. For this, we compared patterns of multipolar chromosome segregation at the first mitosis by labeling specific homologous chromosomes using dCas9-GFP with a specific single-guide RNA (sgRNA) targeting chromosome 9 pericentromere loci (C9-1) (Ma et al., 2015) (Fig. 3A). The C9-1 labeling was in good agreement with that of a chromosome 9 pericentromere-specific FISH probe (Fig. S3A). We also labeled chromosomes and the centrosomes with H2B-mCherry and EGFP-GCP3, respectively (Fig. 3A and S3B; note that C9-1 and the centrosomes were readily distinguished based on their size and relative location to chromosomes).

We found a prominent variation in the numbers of C9-1 foci in each chromosome mass during multipolar chromosome segregation, both in MS- and CF-WGD conditions (Fig. S3C). However, we observed nullisomic chromosome masses that were devoid of C9-1 focus significantly more frequently after MS-WGD than CF-WGD (8.6% or 2.9% upon tripolar segregation and 18% or 9.9% upon tetraploid segregation after MS- or CF-WGD, respectively; Fig. 3B and S3C). We also observed a similar difference in the frequency of nullisomic chromosome masses between MS- and CF-WGD conditions, when chromosome 17 peri-centromeres were labeled by FISH (Fig. 3C and D). Moreover, we observed a similar extent of increase in nullisomic segregation when MS-WGD was induced by the transient co-inhibition of a mitotic kinesin, Eg5, and Mps1 kinase (Fig. S3D; to

suppress SAC with monopolar spindle formation; see Materials and methods for details). These data demonstrate that MS-WGD leads to more frequent nullisomic segregation regardless of either chromosome species or the means of MS induction.

Nullisomy of any chromosome species most likely results in death in the F1 generation. Therefore, we theoretically estimated the viability of F1 cells as the frequency of cells possessing at least one copy of all chromosome species (Fig. 3E). In this estimation, we assumed that the probability of nullisomy formation for all chromosome species was equivalent to that for chromosome 9 (Fig. 3B). The theoretically estimated F1 viability was in good agreement with the actual frequency of viable F1 cells in the live imaging analysis either for MS-WGD or CF-WGD (Fig. 3E). These results suggest that the proneness of MS-WGD-derived F1 cells to nullisomy explains, at least in part, their poorer survivability after multipolar chromosome segregation. An early observation of polyspermic sea urchin embryos suggested that multipolar segregation of homologous chromosomes occurred randomly (Boveri, 1902). In a previous theoretical estimation in human WGD cells, 75% or 23% of F1 cells avoided nullisomy of any homologs upon tripolar or tetrapolar segregation, respectively, assuming all chromosomes to be segregated randomly (Baudoin et al., 2020). The estimated values were closer to those observed after CF-WGD (Fig. 3E), indicating that the homologous chromosome segregation occurred in a non-random manner after MS-WGD.

MS-WGD causes skewed homologous chromosome distribution at the entry into the first mitosis

We asked why nullisomic chromosome segregation occurred more frequently at the first mitosis after MS-WGD than CF-WGD. To address this issue, we compared the fidelity of chromosome capture and segregation between MS- and CF-WGD cells by quantifying the magnitude and frequency of lagging chromosomes or chromosome bridges (Fig. S3E-J). However, MS- and

CF-WGD cells suffered these defects to the equivalent extent, ruling out the fidelity of chromosome segregation as a cause of the difference in nullisomy frequency between these conditions.

As another possible factor affecting nullisomy frequency, we next compared the spatial distribution of homologous chromosomes upon the entry into the first mitosis between MS- and CF-WGD cells by imaging C9-1 along with chromosomes and the centrosomes (Fig. 4A). At this mitotic stage, most WGD cells possessed four C9-1 foci, as sister chromatids had not yet been separated. In CF-WGD cells, two C9-1 foci in each of two nuclei tended to be located distal to each other, resulting in relatively even distributions of the four C9-1 foci (with an average inter-centromere distance of 9.1 μm; Fig. 4A and B; see also Fig. S4A for distributions of inter-centromere distance in each single cell). In sharp contrast, in MS-WGD cells, four C9-1 foci from the single nucleus were often distributed pairwise (Fig. 4A). Accordingly, the frequency of "paired C9-1 foci," defined as those with the inter-centromere distance of < 2 μm, was significantly higher in MS-WGD than in CF-WGD cells (Fig. 4B, C, S4A, and B). These C9-1 pairs were occasionally located proximally from each other, resulting in an overall shorter inter-centromere distance among all four C9-1 foci in MS-WGD cells (on average 6.1 μm; Fig. 4B and S4A). We also compared the spatial distribution of these C9-1 foci between MS- and CF-WGD by quantifying the angles between each two C9-1 foci with regard to the centroid of the whole-chromosome mass (Fig. 4D). The angles were significantly smaller in MS-WGD than in CF-WGD cells (Fig. 4D), reflecting more skewed configurations of homologous centromeres in the former condition.

Using the above images, we also analyzed spatial coordination between each C9-1 foci and the centrosomes. Four centrosomes had already been separated in most MS- and CF-WGD cells around NEBD, often flanking the chromosome masses from their opposite sides (Fig. 4A and S4C). Reflecting the difference in the skewedness of C9-1 distribution, the distance from each centrosome to the closest C9-1 focus was significantly larger with higher deviation in MS-WGD than in

CF-WGD cells (7.0 μm or 5.4 μm in MS- or CF-WGD cells, respectively; Fig. 4E and F; see also Fig. S4D for distributions of the distance in each single cell). Accordingly, we observed "isolated centrosomes" located extremely far (> 10 μm) from any of C9-1 foci more frequently in MS-WGD than in CF-WGD cells (Fig. 4E and G). We also observed the skewed centromere distribution with the frequent centrosome isolation in MS-WGD induced by Eg5 and Mps1 co-inhibition (Fig. S4A-F). These data collectively demonstrate that MS-WGD and CF-WGD differentially impact the geometry of the first mitosis, with the former introducing more skewed homologous chromosome distributions relative to the centrosomes.

Geometric isolation of centrosomes from all homologues drives nullisomic chromosome segregation after MS-WGD

The distally placed centrosomes may have a lower chance of capturing any of the homologous centromeres, possibly explaining the frequent nullisomy after MS-WGD. To test this idea, we traced C9-1 foci and the centrosomes from the entry into the first mitosis until anaphase after MS-WGD by live imaging (Fig. 5A and Video S1). Following the centrosome separation starting before NEBD (Fig. S5A), spatial coordination between C9-1 foci and the centrosomes drastically changed around NEBD (Fig. 5A). As a result, the distance between each C9-1 focus and each centrosome became highly deviated around NEBD (Fig. S5B), which was consistent with the above observation (Fig. 4E, F, and S4D). During chromosome congression at prometaphase, the initial positions of C9-1 foci around the NEBD were well transmitted to their positions within the aligned metaphase plate (Fig. 5A and S5C), consistent with a previous observation in normal mitosis (Gerlich et al., 2003). Upon anaphase onset, each C9-1 focus was separated into two sister foci. Each of these sister foci was segregated toward one of the four centrosomes, enabling us to identify the centrosomes that captured individual sister chromatids in the early mitotic phase (Fig. 5A and S2B). Using this information, we compared distances from C9-1 foci to the centrosomes that

captured these foci with those to the centrosomes that did not capture these foci (Fig. 5B). The former were significantly shorter than the latter from NEBD to the late prometaphase (Fig. 5B). We also analyzed relationship between the C9-1-centrosome distance at NEBD with the frequency of the subsequent capturing of the C9-1 focus by the centrosome (Fig. 5C). A centrosome captured a C9-1 focus at the frequency of >75% when their distance was ≤ 10 μm at NEBD, while the frequency became less than 50% when the distance was > 10 μm (Fig. 5D). Therefore, the initial proximity of the centrosomes to each centromere was linked to a higher chance of their capturing, potentially determining the pattern of subsequent homologue segregation.

To gain further insight into the possible relationship between early centrosome-centromere arrangement and the subsequent formation of nullisomy, we analyzed the time course of the distance from each centrosome to its closest C9-1 focus (Fig. 5D). The centrosomes that did not capture any C9-1 foci located significantly more distant (on average 10 μm) from their closest C9-1 focus than those capturing at least one C9-1 focus (6.8 μm; Fig. 5E). The frequency for a centrosome to undergo nullisomic segregation of C9-1 drastically increased when the distance from the centrosome to the closest C9-1 focus was more than 10 μm (Fig. 5F). Consistent with these quantitative data, visual comparisons of C9-1 and centrosome locations between NEBD and anaphase showed the trend that the centrosomes initially located at the area devoid of C9-1 focus underwent nullisomic segregation at the subsequent anaphase (Fig. 5A and S5C). These results suggest that the initial centrosome-centromere distance is a key determinant of subsequent nullisomy formation.

We reasoned that, if the above assumption was correct, the frequency of nullisomic homologue segregation could be well predicted by the centrosome-centromere distance around NEBD (Fig. 5F). Indeed, the frequency of the nullisomic homologue segregation, which was predicted based on the distance between each centrosome and its closest C9-1 focus around NEBD, well matched with

those obtained by experiments either in MS- or CF-WGD (Fig. 5G, see also Fig. 3B; see Materials and methods for the detail on the equation used). These data collectively support the idea that the proneness of MS-WGD cells to nullisomic homologue segregation is mainly attributed to the skewed homologue distribution at the entry into the first mitosis.

Forced sister chromatid separation in the MS-WGD time window suppresses subsequent nullisomic chromosome segregation

We wished to further address the causality between the skewed homologue distribution and the frequent nullisomic homologue segregation after MS-WGD. To investigate this, we analyzed the intracellular dynamics of C9-1 foci during the progression of MS-WGD to determine how homologous chromosome distribution became skewed during the process (mock-treated control in Fig. 6A; see also S7B). Live imaging revealed that >75% (17 out of 22) sister foci failed to separate upon mitotic exit during MS-WGD (Fig. 6A and B). As a result, the distance between sister C9-1 foci remained on average 1.4 μm at the time when the cells exited mitosis (Fig. 6B). We reasoned that the incomplete sister chromatid separation during MS-WGD potentially skewed homologous chromosome distribution and limited the evenness of their capturing during the subsequent mitosis. To directly test this idea, we attempted to introduce precocious sister chromatid separation by depleting a cohesin subunit, RAD21, during MS-WGD. To avoid pleiotropic damages by long-term loss-of-function of cohesin, we employed the auxin-inducible degron 2 (AID2) technology for depleting RAD21 only in a short time window prior to MS-WGD induction (Fig. 6C) (Yesbolatova et al., 2020). We treated 5-Ph-IAA in RAD21-mAID-Clover (RAD21-mAC) HCT116 cells expressing OsTIR1(F74G) (Yesbolatova et al., 2020) for 2 h (Fig. 6C; see Materials and methods for details), which efficiently degraded RAD21-mAC by the time of MS-WGD induction (Fig. S6A-C). RAD21-mAC degradation induced precocious sister chromatid separation during MS-WGD, resulting in significantly longer distances between sister C9-1 foci after mitotic exit (on

average 2.8 μm; Fig. 6A and B). We then removed 5-Ph-IAA from the cell culture, which allowed the complete restoration of RAD21-mAC expression and sister chromatid cohesion in the subsequent cell cycle right after MS-WGD (Fig. S6B-E).

We next tested the effect of the transient RAD21-mAC depletion before MS-WGD on the subsequent distribution of homologous chromosomes at the first mitosis (Fig. 6C and D). Along with C9-1, chromosomes and the centrosomes were visualized by DAPI and anti-Cep192 immunostaining, respectively. Distance among C9-1 foci tended to be longer with a significant reduction in “paired C9-1 foci” by the transient RAD21-mAC depletion (Fig. 6D-F). The transient RAD21-mAC depletion also significantly increased the inter-C9-1 foci angles, indicating dispersion of homologous centromeres (Fig. 6G). The distance from each centrosome to its closest C9-1 focus tended to be shorter, with a significant reduction in “isolated centrosomes” by the transient RAD21-mAC depletion (Fig. 6H and I). Moreover, the transient RAD21-mAC depletion significantly reduced the frequency of nullisomic segregation of C9-1 foci, both in tripolar and tetrapolar chromosome segregation (Fig. 6J).

As an independent approach, we also induced precocious sister chromatid separation during MS-WGD by RNAi-mediated depletion of Sororin, a cohesin-stabilizing factor (Fig. S7A-C) (Rankin et al., 2005; Schmitz et al., 2007). Similar to the RAD21-mAC depletion, the precocious sister chromatid separation by Sororin depletion led to substantial dispersion of C9-1 foci compared to mock-depleted control at the first mitosis (Fig. S7D-I), with a significant reduction in the frequency of nullisomic segregation in the subsequent anaphase (Fig. S7J). The above data collectively demonstrate that incomplete sister chromatid separation upon MS-WGD is the primary cause of uneven distribution of homologous chromosomes after WGD, facilitating the nullisomy-prone multipolar chromosome segregation in the subsequent mitosis.

Forced sister chromatid separation in the MS-WGD time window improved the viability of the F1 generation

Finally, we determined the causality between the lack of sister chromatid separation upon MS-WGD and the poorer survival of their progenies after multipolar cell division in the subsequent mitosis. For this, we tested the effects of precocious sister chromatid separation during MS-WGD on the subsequent F1 cell viability. Although we initially tried RNAi-mediated Sororin depletion, it resulted in a frequent cell cycle arrest before the entry into the first mitosis (Fig. S7K). This result presumably reflects the deleterious effects of consecutive depletion of Sororin on the progression of the first cell cycle after MS-WGD, precluding us from using this condition for assessing F1 cell viability. Therefore, we next tried the transient RAD21-mAC depletion, with which consecutive loss-of-function of cohesin could be avoided (Fig. S6A-E). We compared F1 cell viability after MS-WGD with or without the transient RAD21-mAC depletion by live imaging (chromosomes were labeled using SiR-DNA dye). The transient RAD21-mAC depletion did not affect the efficiency of the entry to the first mitosis (Fig. S8A), suggesting the absence of considerable damage during the cell cycle after MS-WGD. The polarity of chromosome segregation at the first mitosis was also unaffected by the transient RAD21-mAC depletion (Fig. S8B). However, compared to mock-depleted MS-WGD control, the transient RAD21-mAC depletion significantly increased viable F1 cells that showed DNA content of 2.5-3.5 C or those generated through tripolar chromosome segregation (Fig. 7A, B, and S8C). Total viability of F1 cells was also significantly improved in the transient RAD21-mAC-depleted sample than in the mock-depleted control (Fig. S8D). These results demonstrate that the lack of sister chromatid separation during MS-WGD limits the viability of their progenies, at least in part, through skewing the distribution of chromosome territories and increasing the chance of nullisomic homologue segregation in the subsequent multipolar cell division.

418

Discussion

While WGD occurs through multiple cellular processes, it has been unclear whether the difference in the route of WGD affects the characteristics of the post-WGD cell. We found that the absence or presence of sister chromatid separation upon WGD defined the spatial arrangement of homologous chromosomes in the subsequent cell cycle. Homologous chromosome arrangement then determined the patterns of multipolar chromosome segregation at the first mitosis after WGD, critically affecting the viability of resulting daughter cells. Our findings demonstrate that the difference in geometric properties between MS- and CF-WGD cells had a crucial influence on the proliferative characteristics of their progenies.

Based on our data, we propose the following mechanism of the route-dependent difference in post-WGD cell viability (see Fig. 7C for the schematic model). Due to the absence of sister chromatid separation, MS-WGD leads to more skewed homologue distribution in the subsequent interphase compared to CF-WGD, often with all four homologous chromosomes located on one side of the nucleus (e.g., Fig. 4A, 5A, and S5C; see also Fig. 7C-i). The skewed homologue distribution persists until the entry into the first mitosis, when the separated four centrosomes surround the chromosome mass from all sides (Fig. 7C-ii). This intracellular configuration causes a higher deviation in the centrosome-homologous centromere distance after MS-WGD than CF-WGD, with some centrosomes located particularly distal from any of the homologous centromeres. Our live imaging results suggest that this heterogeneity in the distance from each centrosome to the homologous centromeres has a crucial impact on the efficiency of its homologue capturing: A centrosome placed further than 10 μm from any homologous centromeres at NEBD has a drastically higher chance of nullisomic segregation (Fig. 5F). Interestingly, this threshold distance corresponds well with the length that spindle microtubules can reach during prometaphase in mammalian cells (Piehl and Cassimeris, 2003). Therefore, a centrosome is more likely to lose to other centrosomes in

the “competition” for homologous chromosomes when it is initially isolated from homologous centromeres further than its microtubules can reach (Fig. 7C-iii). We found that the degree of the initial centrosomal isolation well explained the frequency of subsequent nullisomic segregation (Fig. 5F). Moreover, the artificial sister chromatid separation in MS-WGD significantly alleviated the skewed chromosome distribution and reduced nullisomic segregation (Fig. 6 and S7). These results demonstrate that the skewed homologous chromosome arrangement due to the lack of sister chromatid separation is the crucial cause of the higher prevalence of nullisomic chromosome segregation after MS-WGD (Fig. 7C-iv).

The observed F1 cell viability after MS- or CF-WGD matched with the prediction based on the frequency of nullisomic segregation at the first mitosis (Fig. 3E). Moreover, partial resolution of nullisomic segregation by the alleviation of skewed homologue distribution significantly restored F1 cell viability in MS-WGD (Fig. 7A, B, and S8D). These results collectively support the idea that the frequent nullisomy caused by the skewed homologous chromosome distribution is the primary factor that limits the F1 cell viability after MS-WGD. Therefore, the transient intracellular dynamics of sister chromatid separation upon WGD determine the intranuclear organization of post-WGD cells, having a long-term impact on the viability of their progenies through affecting the chromosome segregation patterns in the next cell cycle (Fig. 7C). In other words, sister chromatid separation contributes to “evening out” the intranuclear distribution of homologous chromosomes for facilitating the efficient centrosome-chromosome interactions at mitosis in the next cell cycle, whose significance becomes evident in the geometric condition of post-WGD cells.

The intranuclear homologue distribution immediately after CF-WGD is supposed to be as normal as that of diploids. In contrast, homologue distribution after MS-WGD is skewed and uneven, potentially altering genome-wide gene regulations. We speculate that this difference in intranuclear organization may explain why CF-WGD is a more prevalent form of developmentally programmed

WGD than MS-WGD in different organisms (Chu et al., 2012; Hsu et al., 2016; Rios et al., 2016; Soonpaa et al., 1996). Consistent with this view, a recent study in C. elegans embryos reported that the artificial alteration of the developmentally programmed CF-WGD in intestinal cells to MS-WGD compromised expression of genes required for embryo growth (van Rijnberk et al., 2022). The study proposed that the difference in nuclear surface-to-volume ratio potentially caused the alteration of gene regulations between MS- and CF-WGD. However, considering our findings, MS-WGD-linked alterations in homologous chromosome distribution may also contribute to the observed phenotypes. Interestingly, a recent study reported MS-specific alterations in chromatin organization, which were attributed to the precocious mitotic exit with an abnormally high level of mitotic-specific histone H3 phosphorylation (Gemble et al., 2025). Therefore, several independent principles, including the one found in our study, would critically affect the characteristics of MS-derived cells in parallel. It is an intriguing future study to address the potential impacts of these different principles on the progression of bioprocesses specifically driven by MS.

Fates of post-WGD progenies beyond the F1 generation would be more complicated. We found that the F1 population, regardless of whether they were from MS- or CF-WGD, included either mono-nucleated or bi-nucleated polyploids generated through fusion of multiple daughters (Fig. 2). Therefore, their intranuclear organization is supposed to be more heterogeneous and potentially cluttered compared to that in the P0 cell cycle (i.e., immediately after WGD). For this reason, the difference in the route of WGD would have direct impacts only on the intranuclear organization of P0 cells and chromosome segregation patterns in the first mitosis. However, F1 cells derived from MS- and CF-WGD cells differed not only in the frequency of nullisomy, but also in that of other types of copy number abnormalities, such as monosomy or trisomy (Fig. S3C). Therefore, the initial differences between MS- and CF-WGD cells would be transmitted and have a long-term influence on the characteristics of their progenies in the form of basal karyotypic profiles. It would be intriguing to investigate in the future what karyotypic trends exist in progenies acquired through

different WGD routes.

We demonstrated that artificial induction of sister chromatid separation during MS-WGD significantly improved F1 cell viability. One reason for the limited effect of this rescue approach on F1 viability would be the incompleteness of the sister chromatid separation. The transient removal of cohesin in the absence of an intact mitotic spindle in MS-WGD would not achieve the same scale of sister chromatid separation as that achieved by mechanical segregation mediated by the intact mitotic spindle in CF-WGD. As a result, the resolution of skewed homologue distribution, reduction in the subsequent nullisomic chromosome segregation, and the recovery of F1 viability remained at a modest level in the rescued MS-WGD compared to CF-WGD. However, the apparent correlation between these indices (i.e., the extents of sister chromatid separation, homologue distribution, nullisomy frequency, and F1 viability) strongly supports the idea that the extent of sister chromatid separation is a determining factor of post-WGD cell viability with different routes.

The impacts of differences in WGD routes on subsequent cell viability may also provide an important clue to the control of post-WGD cell populations in cancer therapeutics. Recently, it has been pointed out that anticancer drug treatment often causes artificial induction of WGD in tumors, potentially causing the risk of recurrence through subsequent proliferation of these post-WGD progenies (Conway et al., 2024). Since sister chromatid separation is a key factor affecting post-WGD cell proliferation, suppressing it, for example, through topoisomerase II inhibitors (Downes et al., 1991) could be a potential approach to reduce the risk of post-WGD cell proliferation. Our findings indicate the importance of understanding the differential effects of WGD processes on subsequent cell fates for accurate comprehension of the principle of WGD-driven biological processes and their precise control.

Materials and methods

Cell culture and cell line establishment

HCT116 cells (WT line, RRID: CVCL_0291 from Riken BRC) were cultured in McCoy's 5A (Wako) supplemented with 10% fetal bovine serum (FBS) and 1× antibiotic-antimycotic solution (AA; Sigma-Aldrich) at 37°C with 5% CO_2. Transgenic cell lines were established by transfecting HCT116 cells with plasmids encoding the corresponding transgenes using JETPEI (Polyplus-transfection), followed by selection of positive clones with the appropriate antibiotics. The RAD21-mAC HCT116 cell line expressing OsTIR1(F74G) was a kind gift from Masato Kanemaki (National Institute of Genetics, Japan). Cell lines used in this study are listed in Table S1. All experiments were performed with mycoplasma-free cells (tested by MycoStrip, mycoplasma detection kit; InvivoGen).

Plasmids, compounds, and antibodies

The plasmid vectors constructed or used in this study are listed with the primer information in Table S2. pSpCas9(BB)-2A-GFP (PX458)(Ran et al., 2013), CDNA3.1-dCas9-2xNLS-EGFP (Nelles et al., 2016), and mEOS2-H2B-6 (McKinney et al., 2009) were purchased from Addgene (plasmid #48138, #74710, and #57384, respectively). Compounds and antibodies used in this study are listed in Table S3. The siRNAs used in this study are 5'-GCCUAGGUGUCCUUGAGCUtt-3' (Sororin; DNA in lowercase) and 5'-CGUACGCGGAAUACUUCGAtt-3' (luciferase). siRNA transfection was performed using Lipofectamine RNAiMAX (Thermo Fisher Scientific).

WGD induction

To induce WGD, cells were first arrested at prometaphase by treating with 40 ng/mL nocodazole for 4 h, washing 3 times with supplemented culture medium, and then shaking off. For CF-WGD induction, these shaken-off mitotic cells were treated with 5 μg/mL cytochalasin B for 2 h. For

MS-WGD induction, the shaken-off mitotic cells were co-treated with 40 ng/mL nocodazole and 10 μM RO3306 for 2 h. As an alternative way to induce MS-WGD, cells were arrested at prometaphase by treating with 50 μM monastrol for 4 h, washed 3 times with supplemented culture medium, shaken off, and co-treated with 50 μM monastrol and 5 μM reversine for 2 h. Throughout the manuscript, the time of WGD induction was defined as the time point when these inhibitors for WGD induction were added to cell cultures. After 2-h WGD induction, cells were washed 3 times with supplemented culture medium. The efficiency of WGD induction was evaluated either by the possession of excess centrosomes or the increase in nuclear areas.

For MS-WGD induction in mock- or Sororin-depleted cells, siRNA was transfected at 50 h prior to the induction of MS-WGD. In this case, cells were once arrested at prometaphase by 4-h nocodazole treatment, washed 3 times with supplemented culture medium, and then additionally arrested at metaphase by 2-h MG132 treatment before inducing MS-WGD. For MS-WGD induction in RAD21-mAC cells, 1μg/mL doxycycline and 1 μM 5-Ph-IAA were sequentially administered to the cell culture at 26 h and 2 h prior to MS-WGD induction, respectively. Doxycycline and 5-Ph-IAA were removed when mitotically arrested cells were washed with supplemented culture medium before shake-off.

Colony formation assay and DNA content quantification

For colony formation assay, numbers of the mitotically synchronized cells were counted using hemocytometers right after the mitotic shake off for WGD induction. Then, 2,000 cells were seeded into each well of 6-well dishes to induce either CF-WGD or MS-WGD. After WGD induction, cells were washed 3 times with supplemented medium and further incubated for 8-9 d. Cells forming colonies were live-stained with 10 μg/mL Hoechst 33342 for 30 min at 37°C, subjected to medium change with supplemented phenol red-free McCoy's 5A, and imaged under a Ti2 microscope.

The tile images covering the entire wells were acquired using the Grid/Collection Stitching plugin in μManager software (Edelstein et al., 2014), followed by stitching these tiles using the Image Stitching plugin in FIJI software (NIH). The images of individual colonies were then cropped from the stitched well image, subjected to automated single-nucleus segmentation using the StarDist plugin for quantifying nuclear Hoechst fluorescence intensities of individual cells. The ImageJ macro files used for the automated segmentation are provided as Supplemental material S2. The nuclear Hoechst intensities obtained from an individual colony were plotted into a histogram and subjected to Kernel density estimation to estimate the Hoechst intensity value corresponding to the G1 or G2/M peak. The average G1 Hoechst intensity in diploid control colonies was defined as 2 C. Then, colonies with their G1 Hoechst intensities of more than 3 C were categorized as "polyploid." A single colony consisting of a mixture of diploid and polyploid cell populations was also categorized as polyploid, and its polyploid G1 value was used for the analysis.

Live imaging

For live imaging of the first mitosis after WGD induction, we seeded WGD-induced cells on an 8-well cover glass-bottom chamber (zell-kontakt GmbH), replaced culture media with supplemented phenol red-free McCoy's 5A (Cytiva) at 2 h or 15 h after WGD induction, and started cell imaging from 15 h or 16 h after WGD induction, respectively. For visualizing chromosomes in RAD21-mAC live imaging, 100 nM SiR-DNA (Cytoskeleton, Inc.) was treated 1 h before starting the live imaging. For live imaging of C9-1 foci during MS-WGD induction, the cells arrested at prometaphase were directly subjected to WGD induction without shake-off on an 8-well cover glass-bottom chamber.

Immunostaining

Cells were fixed with 100% methanol at -20°C for 10 min, treated with BSA blocking buffer (150

mM NaCl, 10 mM Tris-HCl, pH 7.5, 5% BSA, and 0.1% Tween 20) for 30 min at 25°C, incubated with the first antibodies overnight at 4°C, and with fluorescence-conjugated secondaries overnight at 4°C. DNA was stained with 1 μg/mL DAPI. Following each treatment, cells were washed 3 times with phosphate-buffered saline (PBS).

Fluorescence in situ hybridization (FISH)

We conducted FISH using ZytoLight FISH-Cytology Implementation kit (ZytoVision GmbH) following the manufacturer's instructions. Cells were treated with the pepsin solution (Cytology Pepsin Solution, ES2, ZytoVision GmbH) or 0.05% pepsin in 10 mM HCl for 10 min at 37°C and fixed with 1% PFA in 1x $MgCl_2$ solution (PT4, ZytoVision GmbH; 1:9 mixture of 10x $MgCl_2$ solution and PBS). The fixed cells were dehydrated with an ethanol series (70, 90, and 100%; for 1 min, each) and air-dried. Samples were then treated with 1x ZytoLight FISH probe solution (ZytoLight CEN 9 Probe or ZytoLight CEN 17 Probe), denatured for 5 min at 72°C, incubated overnight at 37°C, then washed once with 1x Cytology Stringency Wash Buffer SSC (WB7, ZytoVision GmbH) for 2 min at 70°C, and washed once with 1x Cytology Wash Buffer SSC (WB8, ZytoVision GmbH) for 1 min at 25 ˚C. DNA was stained with 1x DAPI/DuraTect-Solution (MT7, ZytoVision GmbH).

Chromosome spread

Cells were treated with 40 ng/mL nocodazole for 4 h at 37°C, collected by trypsinization for 5 min at 37°C, washed twice with PBS, and suspended in 0.056 M KCl. After incubating for 20 min at 25°C, the swollen cells were spun down and fixed with 5 mL of methanol-glacial acetic acid solution (3:1 mixture of methanol and glacial acetic acid) for 20 min on ice. The fixed cell suspension was applied dropwise onto slide glasses from approximately 10 cm above the slides, air dried, and mounted using Fluoromount (Diagnostic BioSystems). Chromosome spreads were stained with 167 nM SYTOX Green.

Quantification of DNA contents in live imaging

To distinguish WGD-induced tetraploids and contaminated (non-WGD-induced) diploids, nuclear areas of individual cells right before the entry to the first mitosis were quantified using automated single-nucleus segmentation by FIJI. Based on the difference in nuclear area between stable diploid and tetraploid control cells (Fig. S2B), we set the threshold of nuclear area between contaminated diploids and WGD-induced tetraploids at 160 μm^2.

To evaluate the validity of F1 cell DNA content estimation based on H2B-mCherry signals, we live-stained MS- or CF-WGD-induced H2B-mCherry cells with 100 ng/mL Hoechst 33342 for 15 min at 37°C and subjected them to live imaging under a Ti2 microscope. Nuclear signals of H2B-mCherry or Hoechst in F1 cells were obtained using automated segmentation by FIJI at the time point when these cells became attached to the dish bottom after the first mitosis. After subtracting the non-cell area background intensities, the DNA content of an individual F1 cell, D_i, was calculated using the equation below, with an assumption that the DNA contents of all sister F1 cells from a single mother cell sum up to 8C:

$$D_i = \frac{8C \times I_i}{\sum I_i}$$

where I_i is the corrected intensity of H2B-mCherry or Hoechst signal in an individual F1 cell. Since the ploidy values estimated by H2B-mCherry signals recapitulated those by Hoechst (Fig. S2F), we used H2B-mCherry signal as an indicator of F1 cell ploidy level in the live imaging analyses. In case of live imaging in RAD21-mAC cells, SiR-DNA signal was used for the ploidy estimation using the above equation.

Quantitative analyses of the centrosome and C9-1 centromere positions in the first mitosis

For analyzing the centrosome and C9-1 centromere position, EGFP-GCP3/dCas9-EGFP (C9-1)/H2B-mCherry cells were observed either by fixed or live cell imaging. For fixed cell imaging, we fixed the WGD-induced cells at 16 h after WGD induction and distinguished the phases of the first mitosis based on the chromosome configuration labeled by H2B-mCherry. The positions of the centrosomes and C9-1 foci were manually measured using the cell counter tool in FIJI. The centroid of the mitotic chromosome masses was measured using FIJI, from the auto-segmented regions of H2B-mCherry signals on the middle slice of Z-sections covering the entire chromosome masses. In live imaging data, three-dimensional positions of the centrosomes and C9-1 were manually measured using the cell counter tool in FIJI.

Microscopy

Fixed cells were observed under either of the following microscopes: A TE2000 microscope (Nikon) equipped with a ×100 1.45 NA Plan-Apochromatic, a CSU-X1 confocal unit (Yokogawa), and an iXon3 electron multiplier-charge coupled device (EMCCD) camera (Andor): A Ti2 microscope (Nikon) with a ×100 1.45 NA Plan-Apochromatic, and Zyla4.2 sCMOS camera (Andor) or ZL41 Cell sCMOS camera (Andor): A Ti microscope (Nikon) with ×100 1.4 NA Plan-Apochromatic, a CSU10 confocal unit (Yokogawa), and an ImagEM (EMCCD) camera (Hamamatsu).

Live cell imaging was conducted under either of the following microscopes at 37°C with 5% CO_2: A TE2000 microscope with x60 1.4 NA Plan-Apochromatic, CSU-X1, and iXon3: A Ti2 microscope with ×20 0.75 NA Plan-Apochromatic, and Zyla4.2: A Ti microscope with a x60 1.4 NA Plan-Apochromatic, CSU10, and ImagEM. Post-WGD cells colonies were observed under a Ti2 microscope with x4 0.13 NA Plan-Fluor and Zyla4.2. Image acquisition was controlled by µManager.

Theoretical modeling of F1 cell viability

F1 cell viability was estimated based on the empirically obtained frequency of nullisomic chromosome segregation of C9-1 at the first mitosis, with the assumptions that 1) nullisomic segregation occurred independently with the same frequency as chromosome 9 for all other chromosome species, and 2) F1 cells were viable when they possessed at least one copy of all chromosome species. Then, the probability of viable F1 cell formation, p_{viable}, was modeled as

$$p_{viable} = \left(1 - p_{nullisomy}\right)^{23},$$

where $p_{nullisomy}$ is the probability of the occurrence of nullisomic segregation of a chromosome species, estimated based on the frequency of nullisomic segregation for chromosome 9. The estimated F1 viability was then expressed as a percentage for comparison with the empirical values obtained by live imaging analysis. Numerical values assigned to the model are listed in Table S4.

Theoretical modeling of nullisomic segregation frequency

Based on the quantitative analysis of live imaging of C9-1 dynamics during the first mitosis (Fig. 5F), we modeled the relationship between the centrosome-centromere distance at NEBD and the frequency of nullisomic homologue segregation at the subsequent anaphase, $f_{nullisomy\ model}$ as

$$f_{nullisomy\ model} = \frac{\sum(N_i \cdot f_i)}{\sum N_i}$$

where N_i is the number of pairs of centrosomes and their closest centromere that falls in each distance bin defined in Fig. 5F, and f_i is the frequency of nullisomic segregation in the corresponding distance bin estimated by the empirical data in Fig. 5F. Model-predicted frequency of

nullisomic segregation was then expressed as a percentage for comparison with the empirical values obtained by imaging analysis. Numerical values assigned to the model are listed in Table S4.

Immunoblotting

Cells were lysed in SDS/PAGE sample buffer (1.125% SDS, 35 mM Tris-HCl, pH 6.8, 11.25% glycerol, 5% 2-mercaptoethanol), boiled for 5 min, and subjected to SDS/PAGE. Separated proteins were transferred onto Immun-Blot PVDF membrane (Bio-Rad). The blotted membranes were blocked with 0.3% skim milk in Tween Tris-buffered saline (TTBS; 50 mM Tris, 138 mM NaCl, 2.7 mM KCl, and 0.1% Tween 20), incubated with the first antibodies for 1 or 2 h at 25 ˚C, or overnight at 4 ˚C, and incubated with horseradish peroxidase (HRP)-conjugated secondary antibodies for 1 or 2 h at 25 ˚C. Each step was followed by 3 washes with TTBS. Signals were detected using the ezWestLumi plus ECL Substrate (ATTO, Tokyo, Japan) with a LuminoGraph II chemiluminescent imaging system (ATTO).

Statistical analysis

Analyses for significant differences between the two groups were conducted using the two-tailed Welch *t*-test, the Fisher exact test, or the Brunner-Munzel test in R software (The R Foundation). Multiple group analyses were conducted using the Fisher exact test with the Benjamini-Hochberg multiple testing correction, the Steel-Dwass test, or the Dwass-Steel Critchlow-Fligner (DSCF) test in R software. Statistical significance was set at $p < 0.05$. *P*-values are indicated in figures or the corresponding figure legends.

Acknowledgment

We are grateful to Masato Kanemaki for providing cell lines, Kinya Yoda for providing antibodies, Saori Takahashi and Ichiro Hiratani for helping with preliminary analyses and valuable comments on the manuscript, Sarah McClelland for valuable suggestions, and the Nikon Imaging Center at Hokkaido University for confocal microscopes. MI and GY are supported by JST SPRING, Grant Number JPMJSP2119. This work was supported by JSPS KAKENHI (Grant Numbers JP19KK0181, JP19H05413, JP19H03219, JPJSBP120193801, JP21K19244, JP22H04926, JP24K21956, JP24KK0139, and JP24K02017 to R.U.), the Princess Takamatsu Cancer Research Fund, the Kato Memorial Bioscience Foundation, the Orange Foundation, the Smoking Research Foundation, Daiichi Sankyo Foundation of Life Science, the Akiyama Life Science Foundation, the Hoansha Foundation, Sumitomo Electric Group CSR Foundation, and the Terumo Life Science Foundation to R.U. The authors declare no competing financial interests.

Author Contributions

Conceptualization, M.I., and R.U.; Methodology, M.I., G.Y., Y.T., and R.U.; Investigation, M.I.; Formal Analysis, M.I., and R.U.; Resources, M.I., G.Y., Y.T., and R.U.; Supervision, R.U.; Writing – Original Draft, R.U.; Writing – Review & Editing, M.I., and R.U.; Funding Acquisition, M.I., G.Y., Y.T., and R.U.

Figure legends

Figure 1. Less efficient cell proliferation after MS-WGD than CF-WGD

(A) A schematic image of the schedule for MS- or CF-WGD induction. **(B)** Fluorescence microscopy of an MS- or CF-WGD-induced cell. The centrosomes were stained with anti-Cep192. DNA was stained with DAPI. Cells were fixed at 4 h after WGD induction. Insets show 3x enlarged images of the centrosomes. Broken lines indicate cell contours. **(C)** Fluorescence microscopy of Hoechst33342-stained colonies formed after WGD induction. The entire views of culture dish wells (left) or enlarged images of single colonies (right). Mock treatment control without WGD induction is shown on top (non-WGD). **(D)** Histograms of DNA content distribution in single colonies in C. DNA content was quantified based on Hoechst33342 signal in each cell within the colonies. Blue lines indicate the estimated G1 DNA content values. All analyzed data are provided in Supplemental material S1. **(E)** Ploidy levels of individual colonies in C, calculated by normalizing the G1 DNA content of each colony to the average G1 DNA content of the diploid control. At least 355 colonies from six replicates from three independent experiments were analyzed for MS- or CF-WGD samples. Thirty-two colonies from three independent experiments were analyzed for diploid control. Colonies with normalized G1 DNA content of > 3 C were defined as "polyploid." **(F)** Number of polyploid colonies per well in each WGD condition. Means ± s.e. of six replicates from three independent experiments. Asterisks indicate statistically significant difference between conditions (**$p < 0.01$, the Brunner-Munzel test).

Figure 2. Poorer survival of MS-WGD cells through multipolar chromosome segregation at the first mitosis

(A) A schematic image of the schedule for WGD induction and live imaging. **(B)** Time-lapse images of H2B-mCherry cells during the first mitosis after CF-WGD. Images were taken at 10-min intervals. The timing of NEBD is set as 0 min. White arrowheads indicate "unfused" daughter cells.

The yellow arrow indicates a binucleated cell formed through the fusion of two daughter cells at the end of the first mitosis. Images of MS-WGD cells are shown in Fig. S2C. **(C)** Frequency of chromosome segregation polarity at the first mitosis in Fig. 2B and S2C. Means ± s.e. of three independent experiments. At least 108 cells were analyzed in each condition. There is no statistically significant difference between conditions (p = 0.49, the Fisher exact test). **(D)** An example of the estimation of daughter cell DNA content based on the segregation ratio of H2B-mCherry signal at the first mitosis. For the demonstration, an identical cell to the "tetrapolar" cell in B is shown. **(E)** Estimated DNA content (C-value) in individual F1 cells in B. Data are sorted according to the prolife of the first mitosis (chromosome segregation polarity and the presence or absence of daughter cell fusion) that formed the corresponding F1 cells. Individual F1 cells are labeled in different colors based on their fates. At least 257 cells from three independent experiments were analyzed. **(F, G)** Viability (proportion of "divided" cells) of F1 cells, sorted by DNA content of individual F1 cells (F) or the polarity of chromosome segregation at the first mitosis (G). Means ± s.e. of three independent experiments. At least 55 or 28 cells were analyzed in each bin (F) or polarity (G), respectively. Only unfused F1 cells were used for the quantification in G. Asterisks indicate statistically significant difference between conditions (n.s.: not significant, ***$p < 0.001$, the Brunner-Munzel test).

Figure 3. More frequent nullisomic chromosome segregation occurs at the first mitosis after MS-WGD than CF-WGD

(A, C) Fluorescence microscopy of anaphase cells at the first mitosis after MS- or CF-WGD. The centrosomes, centromeres of chromosome 9, and chromosomes were labeled by EGFP-GCP3, dCas9-EGFP with specific sgRNA (C9-1), and H2B-mCherry, respectively, in A. Identical images with indications of the centrosome positions are shown in Fig. S3B. Centromeres of chromosome 17 and chromosomes were stained with a specific FISH probe and DAPI, respectively, in C. Yellow arrowheads indicate the centromeres. Orange arrows indicate a chromosome mass devoid of the

labeled homologous centromeres (nullisomy). Broken lines indicate the contours of chromosome masses. **(B, D)** Frequency of the segregated chromosome masses devoid of any centromere signals for chromosome 9 (B) or 17 (D) in A or C, respectively. Means ± s.e. of three independent experiments. At least 252 or 172 segregated chromosome masses (presumptive daughter nuclei) were analyzed in each polarity in B or D, respectively. Asterisks indicate statistically significant difference between conditions (***$p < 0.001$, the Brunner-Munzel test). **(E)** Comparison between the model-predicted and empirical viability of F1 cells after MS- or CF-WGD. See Materials and methods for details of the model prediction. The empirical data are identical to those in Fig. 2G (shown for enabling the direct comparison).

Figure 4. Skewed distribution of homologous centromeres in the first mitosis after MS-WGD

(A) Fluorescence microscopy of cells at the entry into the first mitosis after MS- or CF-WGD. The centrosomes, centromeres of chromosome 9, and chromosomes were labeled by EGFP-GCP3, dCas9-EGFP with specific sgRNA (C9-1), and H2B-mCherry, respectively. White arrows and yellow arrowheads indicate the centrosomes and C9-1 centromeres, respectively. **(B)** Histogram of inter-centromere distance in A. Six inter-centromere distances among the 4 C9-1 foci were obtained from each cell. At least 414 C9-1 centromere combinations from at least 69 cells from three independent experiments were analyzed. C9-1 combinations with their distance less than 2 μm (defined as “paired centromeres”) are indicated by the blue arrow. Asterisks indicate statistically significant difference between conditions (***$p < 0.001$, the Welch’s t-test). **(C)** Frequency of paired C9-1 centromeres in B. Means ± s.e. of three independent experiments. Asterisks indicate statistically significant difference between conditions (***$p < 0.001$, the Brunner-Munzel test). **(D)** Left: An example of the inter-centromere angle quantification. For the demonstration, the identical CF-WGD cell in A is shown. Right: Histogram of the angles between two C9-1 foci with regard to the centroid of the whole-chromosome mass in A. At least 354 C9-1 combinations from at least 59 cells from three independent experiments were analyzed. Asterisks indicate statistically significant

difference between conditions (***$p < 0.001$, the Welch's t-test). **(E)** Left: Schematic images of the closest centrosome-centromere distance with skewed or more even homologous centromere distributions. Right: Histogram of the distance from each centrosome to its closest C9-1 focus in A. Four centrosome-centromere distances were obtained from an individual cell. The centrosome-centromere combinations whose distances exceeded 10 μm (defined as "isolated centrosomes") are indicated by the green arrow. At least 276 centrosome-centromere combinations from at least 69 cells from three independent experiments were analyzed. Asterisks indicate statistically significant difference between conditions (***$p < 0.001$, the Welch's t-test). **(F)** Standard deviation of the closest centrosome-centromere distances in each cell in E. Asterisks indicate statistically significant difference between conditions (***$p < 0.001$, Welch's t-test). **(G)** Frequency of isolated centrosomes in E. Means ± s.e. of three independent experiments. Asterisks indicate statistically significant difference between conditions (***$p < 0.001$, the Brunner-Munzel test).

Figure 5. Geometric isolation of centrosomes drives nullisomic chromosome segregation after MS-WGD

(A) Time-lapse images of H2B-mCherry, EGFP-GCP3, and dCas9-EGFP with C9-1 sgRNA throughout the first mitosis after MS-WGD. Images were taken at 5-min intervals. The timing of NEBD is set as 0 min. Yellow arrowheads or white arrows indicate centromeres or centrosomes, respectively. The yellow circle indicates a chromosome mass devoid of any C9-1 foci. Individual centrosomes were distinguished by labeling different letters (a-d). **(B)** The centrosome-centromere distance of captured or uncaptured pairs in A. Means ± s.d. of at least 114 centrosome-centromere pairs from 19 cells from five independent experiments. Asterisks indicate statistically significant difference between conditions throughout mitosis (0-30 min after NEBD; ***$p < 0.001$, the Welch's t-test). **(C)** The frequency of centrosome-centromere capturing, which was calculated for each bin of the initial centrosome-centromere distance (schematized on the left). Three hundred four

centrosome-centromere pairs from 19 cells from five independent experiments were analyzed. **(D)** The time course of the distance from each centrosome to its closest C9-1 focus (schematized on left) in the cell shown in A. The asterisk indicates a centrosome that failed to capture any of the C9-1 foci. **(E)** The initial distance (at NEBD) to the closest C9-1 focus from centrosomes that captured at least one C9-1 focus (non-nullisomic) or those that did not capture any foci (nullisomic). Means ± s.d. of at least 14 centrosomes from 19 cells from five independent experiments. Asterisks indicate statistically significant difference between conditions (***$p < 0.001$, the Welch's t-test). **(F)** The frequency of the centrosomes that underwent nullisomic C9-1 segregation, which was calculated for each bin of the closest centrosome-centromere distance at NEBD (schematized on the left). At least 76 centrosomes from 19 cells from five independent experiments were analyzed. **(G)** Comparison between the model-predicted and empirical frequency of segregated chromosome masses devoid of any C9-1 foci in tetrapolar chromosome segregation at the first mitosis after MS- or CF-WGD. See Materials and methods for details of the model prediction. The empirical data are identical to those in Fig. 3B (shown for enabling the direct comparison). Means ± s.e. of three independent experiments. Asterisks indicate statistically significant difference between conditions (***$p < 0.001$, the Brunner-Munzel test).

Figure 6. Suppression of nullisomic homologue segregation at the first mitosis by artificial sister chromatid separation upon MS-WGD

(A) Time-lapse images of dCas9-EGFP with C9-1 sgRNA and chromosomes stained with SiR-DNA during MS-WGD in RAD21-mAC cells treated with or without 5-Ph-IAA. Images were taken at 6-min intervals. The time after starting WGD induction was indicated. White arrowheads indicate C9-1 foci. **(B)** Time course of inter-sister chromatid distance in A. Means ± s.d. of at least 22 sister chromatid pairs from at least 11 cells from two independent experiments. Asterisks indicate statistically significant difference between conditions at the last time point (**$p < 0.01$, the Welch's t-test). **(C)** A schematic image of the schedule for AID2-mediated transient depletion of RAD21

before MS-WGD induction. **(D)** Fluorescence microscopy of cells at the entry into the first mitosis after MS-WGD in RAD21-mAC cells treated with or without 5-Ph-IAA. The centrosomes, C9-1 centromeres, and chromosomes were labeled by immunostaining of Cep192, expression of dCas9-EGFP with a targeting sgRNA, and DAPI staining, respectively. **(E, H)** Histogram of inter-centromere distance (E) or the distance from each centrosome to its closest C9-1 focus (H). At least 168 C9-1 combinations (E) or at least 112 centrosome-C9-1 combinations (H) from at least 28 cells from three independent experiments were analyzed. There is no statistically significant difference between conditions (*p* values of the Welch's t-test are shown). **(F, I)** Frequency of paired C9-1 centromeres (F) or isolated centrosomes (I) in E or H, respectively. Means ± s.e. of three independent experiments. Asterisks indicate statistically significant difference between conditions (***$p < 0.001$, the Brunner-Munzel test). **(G)** Quantification of the angles between each two C9-1 foci with regard to the centroid of the whole-chromosome mass. At least 168 C9-1 combinations from at least 28 cells from three independent experiments were analyzed. There is a statistically significant difference between conditions (*$p < 0.05$, the Welch's t-test). **(J)** Frequency of C9-1 nullisomic chromosome segregation during anaphase at the first mitosis after MS-WGD with or without the transient RAD21-mAC depletion. Means ± s.e. of three independent experiments. At least 150 segregated chromosome masses from at least 50 cells from three independent experiments were analyzed in each polarity. Asterisks indicate statistically significant difference between conditions (***$p < 0.001$, the Brunner-Munzel test).

Figure 7. Improvement of F1 cell viability by artificial sister chromatid separation upon MS-WGD

(A, B) Viability of F1 cells in live imaging analysis after MS-WGD with or without the transient RAD21 depletion. Data are sorted by ploidy of individual F1 cells (A) or the polarity of chromosome segregation at the first mitosis (B). Means ± s.e. of three independent experiments. At least 59 or 30 cells were analyzed in each bin (A) or polarity (B), respectively. Only unfused F1

cells were used for the quantification in B. Asterisks indicate statistically significant difference between conditions (n.s.: not significant, ***$p < 0.001$, the Brunner-Munzel test). **(C)** A model for the route-dependent difference in post-WGD progenies. While sufficient separation of sister chromatids establishes even distribution of homologous chromosomes in the first cell cycle after CF-WGD, the lack of sister chromatid separation causes more skewed homologue distribution after MS-WGD (i). This difference in homologue arrangement results in greater variation in centrosome-centromere distance upon entry into the first mitosis after MS-WGD than CF-WGD (ii). Presumably because of the limited reach length of centrosomal microtubules, centrosomes apart from any of homologous centromeres further than 10 μm have a high chance of failure in capturing any of these homologues ("Loser" centrosome, iii). These geometric characteristics of post-MS-WGD cells cause frequent nullisomy in F1 cells, limiting the viability of post-WGD progenies compared to CF-WGD.

Figure S1. Evaluation of the efficiency of WGD induction

(A) Quantification of DNA content and the possession of excess (>2) centrosomes in WGD-induced cell cultures. WGD cells were defined based on the possession of excess centrosomes (red dots; the centrosomes were marked by Cep192 as depicted in Fig. 1B). Note that the substantial overlap in DNA contents between diploids (black dots) and WGD cells is presumably due to the asynchronous cell cycle stage distributions in the former. **(B)** Efficiency of WGD induction in A. Means ± s.e. of three independent experiments. At least 292 cells were analyzed in each condition. There is no statistically significant difference between conditions ($p = 0.87$, the Brunner-Munzel test). **(C)** Frequency of nuclear numbers in WGD-induced cells at the first cell cycle after MS- or CF-WGD. Pooled data from at least 235 cells from three independent experiments are shown. **(D)** A comparison of the number of colonies formed from untreated diploids (left) and that of diploid cell colonies formed after MS- or CF-WGD induction in Fig. 1C (right). The number of untreated diploids initially seeded was determined based on the estimated number of contaminated diploids in

B. Data were obtained from 3 independent experiments with two replicates each.

Figure S2. Live imaging of the first mitosis and F1 cell cycle after MS- or CF-WGD

(A) Fates of P0 cells (the first cell cycle) after MS- or CF-WGD induction. At least 161 cells from three independent experiments were analyzed. There is no statistically significant difference between conditions (p = 0.91, the Fisher exact test). **(B)** Quantification of nuclear areas in diploid, stable tetraploids, or MS- or CF-WGD-induced cells immediately before the entry into mitosis (the first mitosis in case of the WGD-induced cells). Diploid and tetraploid cells were clearly distinguished based on the nuclear area. Therefore, cells with nuclear areas of > 160 μm^2 (the broken line) were defined as WGD-induced cells in the MS- or CF-WGD condition. At least 41 cells from at least two independent experiments were analyzed. **(C)** Time-lapse images of H2B-mCherry cells during the first mitosis after MS-WGD. Images were taken at 10-min intervals. The timing of NEBD is set as 0 min. White arrowheads indicate "unfused" daughter cells formed through the first mitosis. The yellow arrow indicates a "fused" binucleated daughter cell. **(D)** Mitotic duration from NEBD to anaphase onset at the first mitosis after MS- or CF-WGD in Fig. 2B and S2C. Means ± s.d. of at least 108 cells from three independent experiments. There is no statistically significant difference between conditions (p = 0.054, the Welch's t-test). **(E)** Fluorescence microscopy of a CF-WGD-induced H2B-mCherry cells stained with Hoechst 33342 (at 16 h after WGD-induction). **(F)** Relationship between the DNA content of F1 daughter cells estimated based on the signal segregation ratio of Hoechst or H2B-mCherry. DNA content estimation was conducted as depicted in Fig. 2D. The Correlation coefficient between the variables is shown. **(G)** Frequency of daughter cell fusion at the first mitosis after MS- or CF-WGD in Fig. 2B and S2C. At least 28 cells from three independent experiments were analyzed in each polarity. **(H)** Time-lapse images of H2B-mCherry cells during the F1 cell cycle after MS-WGD. Images were taken at 10-min intervals. Dividing daughter cells indicated by arrowheads are traced in the subsequent time frames. The timing of anaphase onset is set as 0 min. The panels with asterisks

show an identical dividing mother cell whose different daughters are traced in the subsequent time frames in different rows. **(I, J)** Frequency of cell fate (I) or viability of F1 generation that was sorted based on the presence or absence of daughter cell fusion after multipolarization (J) in the live imaging in Fig. 2B and S2C. Means ± s.e. of three independent experiments. At least 55 cells (I) or 28 cells (J) were analyzed in each category. Asterisks indicate statistically significant difference between conditions (n.s.: not significant, ***$p < 0.001$, the Brunner-Munzel test in I, or the Steel-Dwass test in J).

Figure S3. Imaging analyses for multipolar chromosome segregation patterns after WGD

(A) Comparison of chromosome 9 centromere labeling with dCas9-EGFP (left; imaged before cell fixation) and that with a specific FISH probe (right; imaged after cell fixation) in diploid interphase cells. Fluorescence microscopy of identical cells before and after cell fixation. DNA was stained with DAPI after fixation. Note that dCas9-EGFP, EGFP-GCP3, and H2B-mCherry signals observed in the pre-fixed sample were breached in the process of cell fixation for FISH staining. **(B)** Fluorescence microscopy of anaphase cells at the first mitosis after MS- or CF-WGD. The centrosomes (white arrows), centromeres of chromosome 9 (yellow arrowheads), and chromosomes were labeled by EGFP-GCP3, dCas9-EGFP with specific sgRNA (C9-1), and H2B-mCherry, respectively. For the demonstration, identical cells are shown in Fig. 3A. **(C)** Histograms of C9-1 foci numbers detected in segregated chromosome masses in anaphase in Fig. 3A. Means ± s.e. of three independent experiments. At least 84 cells were analyzed in each condition. Asterisks indicate statistically significant difference between MS- and CF-WGD in each category (n.s.: not significant, ***$p < 0.001$, the Brunner-Munzel test). **(D)** The proportion of segregated chromosome masses devoid of any C9-1 focus. Means ± s.e. of three independent experiments. At least 252 segregated chromosome masses (presumptive daughter nuclei) were analyzed in each polarity. Asterisks indicate statistically significant difference between conditions (n.s.: not significant, ***$p < 0.001$, the Steel-Dwass test). Identical data to those in Fig. 3B are shown for MS-WGD (Noc+RO) and

CF-WGD for comparison with the MS-WGD (Mon+Rev) condition. **(E, H)** Fluorescence microscopy of H2B-mCherry and the kinetochores (immunostained CENP-E in E) or spindle microtubules (β-tubulin in H) in anaphase at the first mitosis after CF-WGD. The right panel in E shows a 3x enlarged image of a lagging chromosome. The yellow arrowhead indicates a chromosome bridge in H. **(F, I)** Numbers of lagging chromosomes (F) or chromosome bridges (I) found in each cell in E or H, respectively. There is no statistically significant difference between conditions in F or I (p = 0.14 or p = 0.39, respectively, the Welch's t-test). At least 39 cells from three independent experiments were analyzed in each condition. **(G, J)** Frequency of anaphase cells with at least one lagging chromosome (G) or chromosome bridge (J) in E or H, respectively. Means ± s.e. of three independent experiments. At least 39 cells were analyzed in each condition. There is no statistically significant difference between conditions in G or J (p = 0.67 or p = 0.55, respectively, the Brunner-Munzel test).

Figure S4. Homologue distribution is commonly skewed after MS-WGD induced by different methods

(A, C, D) Quantification of inter-centromere distance (A), inter-centrosome distance (C), or the distance from each centrosome to its closest centromere (D) at the entry into the first mitosis after MS- or CF-WGD. Each column represents the distances obtained in an individual cell. Paired centromeres or isolated centrosomes are colored in blue (A) or green (D), respectively. At least 60 cells from three independent experiments were analyzed. **(B, F)** Frequency of paired C9-1 centromeres (B) or isolated centrosomes (F) in A or D, respectively. Means ± s.e. of three independent experiments. Asterisks indicate statistically significant difference between conditions (n.s.: not significant, ***p < 0.001, the Steel-Dwass test). **(E)** Standard deviation of the distances in each cell in D. Asterisks indicate statistically significant difference between conditions (n.s.: not significant, ***p < 0.001, the DSCF test). Identical data to those in Fig. 4C, F, or G are shown for MS-WGD (Noc+RO) and CF-WGD in B, E, or F, respectively, for comparison with MS-WGD

(Mon+Rev) condition.

Figure S5. Quantitative analysis of centromere and centrosome dynamics during the first mitosis after MS-WGD

(A) Examples of the time course of inter-centrosome distance in Fig. 5A. Broken lines indicate the timing of NEBD or anaphase onset (black or gray, respectively). The asterisk indicates a clustered centrosomal pair. **(B)** Examples of the time course of distance between each centrosome-centromere combination in Fig. 5A. Each graph represents the distances from a single C9-1 focus to all 4 centrosomes (a-d). Asterisks indicate the centrosomes that did not capture the corresponding centromere. **(C)** Time-lapse images of H2B-mCherry, EGFP-GCP3, and dCas9-EGFP with C9-1 sgRNA throughout the first mitosis after MS-WGD. Yellow arrowheads indicate centromeres. White arrows and orange arrows indicate centrosomes with and without capturing C9-1 foci, respectively. Asterisks indicate C9-1 foci in neighbor cells.

Figure S6. Artificial induction of sister chromatid separation in a short time window upon MS-WGD by transient RAD21-mAC depletion

(A) A schematic image of the schedule for AID2-mediated transient depletion of RAD21 before MS-WGD induction. **(B)** Immunoblotting of RAD21 in RAD21-mAC cells treated with or without 5-Ph-IAA. RAD21 expression before or 16 h after washout of 5-Ph-IAA was tested. β-tubulin was detected as a loading control. **(C)** Quantification of the relative intensity of RAD21 in B. Protein loading differences were corrected based on β-tubulin signals. Mean ± s.e. of three independent experiments. Asterisks indicate statistically significant differences among conditions (n.s.: not significant, ***$p < 0.001$, the Steel-Dwass test). **(D)** Chromosome spreads that were prepared from the cells undergoing MS-WGD (0 h) or the first mitosis after MS-WGD (16 h). While AID2-mediated depletion of RAD21 resulted in precocious separation of sister chromatids during MS-WGD, subsequent removal of 5-Ph-IAA allowed sister chromatid cohesion to be restored and

maintained at the prometaphase in the first mitosis after MS-WGD. DNA was stained with SYTOX green. **(E)** Frequency of chromosome spreads with separated or cohesed sister chromatid pairs in D. Mean ± s.e. of three independent experiments. At least 53 cells were analyzed in each condition. Asterisks indicate statistically significant differences among conditions (n.s.: not significant, ***p < 0.001, the Fisher exact test).

Figure S7. Artificial induction of sister chromatid separation by RNAi-mediated Sororin depletion

(A) Immunoblotting of Sororin in mock- or Sororin-depleted cells sampled at the timing of MS-WGD induction. β-tubulin was detected as a loading control. **(B)** Time-lapse images of H2B-mCherry, EGFP-GCP3, and dCas9-EGFP with C9-1 sgRNA during MS-WGD in mock- or Sororin-depleted cells. Images were taken at 6-min intervals. The timing of starting WGD induction was set as 0 min. White arrows and yellow arrowheads indicate the centrosomes and C9-1 centromeres, respectively. **(C)** Time course of inter-sister chromatid distance in B. Means ± s.d. of at least 14 sister chromatid pairs from at least 7 cells from two independent experiments. Asterisks indicate statistically significant difference between conditions at the last time point (**p < 0.01, the Welch's t-test). **(D)** Fluorescence microscopy of cells at the entry into the first mitosis after MS-WGD in mock- or Sororin-depleted cells. White arrows and yellow arrowheads indicate the centrosomes and C9-1 centromeres, respectively. **(E)** Histogram of inter-centromere distance in D. Six inter-centromere distances were obtained from the 4 C9-1 foci in an individual cell. At least 258 C9-1 combinations from 43 cells from three independent experiments were analyzed. Asterisks indicate statistically significant difference between conditions (***p < 0.001, the Welch's t-test). **(F)** Frequency of paired C9-1 centromeres in E. Means ± s.e. of three independent experiments. Asterisks indicate statistically significant difference between conditions (***p < 0.001, the Brunner-Munzel test). **(G)** Quantification of the angles between each two C9-1 foci with regard to the centroid of the whole-chromosome mass in C. At least 216 C9-1 combinations from at least 36

cells from three independent experiments were analyzed. There is a statistically significant difference between conditions (*$p < 0.05$, the Welch's t-test). **(H)** Histogram of the distance from each centrosome to its closest C9-1 focus in C. Four centrosome-centromere distances were obtained from an individual cell. At least 172 centrosome-centromere combinations from 43 cells from three independent experiments were analyzed. Asterisks indicate statistically significant difference between conditions (***$p < 0.001$, the Welch's t-test). **(I)** Frequency of isolated centrosomes in H. Means ± s.e. of three independent experiments. P-value obtained by the Brunner-Munzel test between conditions is shown on top. **(J)** Frequency of C9-1 nullisomic chromosome segregation during anaphase at the first mitosis after MS-WGD in mock- or Sororin-depleted cells. Means ± s.e. of three independent experiments. At least 102 segregated chromosome masses from at least 34 cells from three independent experiments were analyzed in each polarity. Asterisks indicate statistically significant difference between conditions (***$p < 0.001$, the Brunner-Munzel test). **(K)** Fates of P0 cells (the first cell cycle) after MS-WGD induction in mock- or Sororin-depleted cells. At least 75 cells from two independent experiments were analyzed. Asterisks indicate statistically significant difference between conditions (***$p < 0.001$, the Fisher exact test).

Figure S8. Artificial induction of sister chromatid separation by transient RAD21-mAC depletion improves F1 cell viability after MS-WGD

(A-D) Fates of P0 cells (A), frequency of chromosome segregation polarity at first mitosis (B), estimated DNA content (c-value) in individual F1 cells (C), or viability of F1 cells (D) after MS-WGD induction in RAD21-mAC cells treated with or without 5-Ph-IAA. Means ± s.e. of three independent experiments in B or D. At least 206 cells (A), 133 cells (B), and 317 cells (C, D) from three independent experiments were analyzed. There is no statistically significant difference between conditions in A or B ($p = 0.94$ or $p = 0.88$, respectively, the Fisher exact test). Asterisks indicate statistically significant difference between conditions in D (***$p < 0.001$, the

Brunner-Munzel test).

Figure S9. Original immunoblot membranes used for the analyses

Uncropped images of all Western blots are shown, with the approximate indications of the cropped regions.

Video S1. The dynamics of homologous centromeres and the centrosomes during the first mitosis after MS-WGD

Fluorescence microscopy (maximum z-projections of confocal images) of the first mitosis after MS-WGD. The centrosomes, centromeres of chromosome 9, and chromosomes were labeled by EGFP-EGP3, dCas9-EGFP with specific sgRNA (C9-1), and H2B-mCherry, respectively. Individual centrosomes or centromeres were distinguished by labeling different letters (a-d) or numbers (1-4), respectively. The movie is shown at 600x real-time. Time is indicated as hour: min. Scale bar: 10 µm.

Table S1. List of cell lines used in this study

Table S2. List of plasmids used in this study

Table S3. List of antibodies and compounds used in this study

Table S4. Numerical values assigned to the models

Supplemental material S1. DNA contents in all colonies analyzed in Figure 1

Histograms of DNA content distribution in all colonies analyzed for Fig. 1E and F. DNA contents were quantified based on Hoechst33342 signal in each cell within the colonies. Blue lines indicate

the estimated G1 DNA content values.

Supplemental material S2. The ImageJ macro files used for the automated segmentation

References

Aylon, Y., and M. Oren. 2011. p53: Guardian of ploidy. *Molecular Oncology*. 5:315-323.

Baudoin, N.C., J.M. Nicholson, K. Soto, O. Martin, J. Chen, and D. Cimini. 2020. Asymmetric clustering of centrosomes defines the early evolution of tetraploid cells. *Elife*. 9.

Bernhard, S.V., S. Gemble, R. Basto, and Z. Storchova. 2023. Experimental Approaches to Generate and Isolate Human Tetraploid Cells. *In* Polyploidy: Methods and Protocols. Y. Van de Peer, editor. Springer US, New York, NY. 391-399.

Boveri, T. 1902. Über mehrpolige Mitosen als Mittel zur Analyse des Zellkerns. Stuber.

Boveri, T. 1914. Zur frage der entstehung maligner tumoren. Gustav Fischer.

Brito, D.A., and C.L. Rieder. 2006. Mitotic Checkpoint Slippage in Humans Occurs via Cyclin B Destruction in the Presence of an Active Checkpoint. *Current Biology*. 16:1194-1200.

Chu, L.T., S.H. Fong, I. Kondrychyn, S.L. Loh, Z. Ye, and V. Korzh. 2012. Yolk syncytial layer formation is a failure of cytokinesis mediated by Rock1 function in the early zebrafish embryo. *Biol Open*. 1:747-753.

Conway, P.J., J. Dao, D. Kovalskyy, D. Mahadevan, and E. Dray. 2024. Polyploidy in Cancer: Causal Mechanisms, Cancer-Specific Consequences, and Emerging Treatments. *Mol Cancer Ther*. 23:638-647.

Crockford, A., L.P. Zalmas, E. Grönroos, S.M. Dewhurst, N. McGranahan, M.E. Cuomo, V. Encheva, A.P. Snijders, J. Begum, S. Purewal, J. Cerveira, H. Patel, M.J. Renshaw, and C. Swanton. 2017. Cyclin D mediates tolerance of genome-doubling in cancers with functional p53. *Ann Oncol*. 28:149-156.

Darmasaputra, G.S., L.M. van Rijnberk, and M. Galli. 2024. Functional consequences of somatic polyploidy in development. *Development*. 151.

Darp, R., M.A. Vittoria, N.J. Ganem, and C.J. Ceol. 2022. Oncogenic BRAF induces whole-genome doubling through suppression of cytokinesis. *Nat Commun*. 13:4109.

Duncan, A.W., A.E. Hanlon Newell, L. Smith, E.M. Wilson, S.B. Olson, M.J. Thayer, S.C. Strom, and M. Grompe. 2012. Frequent Aneuploidy Among Normal Human Hepatocytes. *Gastroenterology*. 142:25-28.

Edelstein, A.D., M.A. Tsuchida, N. Amodaj, H. Pinkard, R.D. Vale, and N. Stuurman. 2014. Advanced methods of microscope control using μManager software. *J Biol Methods*. 1.

Fava, L.L., F. Schuler, V. Sladky, M.D. Haschka, C. Soratroi, L. Eiterer, E. Demetz, G. Weiss, S. Geley, E.A. Nigg, and A. Villunger. 2017. The PIDDosome activates p53 in response to supernumerary centrosomes. *Genes Dev*. 31:34-45.

Ganem, Neil J., H. Cornils, S.-Y. Chiu, Kevin P. O'Rourke, J. Arnaud, D. Yimlamai, M. Théry, Fernando D. Camargo, and D. Pellman. 2014. Cytokinesis Failure Triggers Hippo Tumor Suppressor Pathway Activation. *Cell*. 158:833-848.

Ganem, N.J., S.A. Godinho, and D. Pellman. 2009. A mechanism linking extra centrosomes to chromosomal instability. *Nature*. 460:278-282.

Gemble, S., M. Budzyk, A. Simon, R. Lambuta, N. Weiss, A. Forest, Y. Miroshnikova, F. Scotto Di Carlo, V. Marthiens, C. Verdel, J. Fang, C. Desdouets, S. Wickström, G. Ciriello, E. Oricchio, G. Almouzni, and R. Basto. 2025. Mitotic slippage causes nuclear instability in polyploid cells. *bioRxiv*:2025.2007.2021.665898.

Gerlich, D., J. Beaudouin, B. Kalbfuss, N. Daigle, R. Eils, and J. Ellenberg. 2003. Global Chromosome Positions Are Transmitted through Mitosis in Mammalian Cells. *Cell*. 112:751-764.

Gisselsson, D., U. Håkanson, P. Stoller, D. Marti, Y. Jin, A.H. Rosengren, Y. Stewénius, F. Kahl, and I. Panagopoulos. 2008. When the genome plays dice: circumvention of the spindle assembly checkpoint and near-random chromosome segregation in multipolar cancer cell mitoses. *PLoS One*. 3:e1871.

Gisselsson, D., Y. Jin, D. Lindgren, J. Persson, L. Gisselsson, S. Hanks, D. Sehic, L.H. Mengelbier, I. Øra, N. Rahman, F. Mertens, F. Mitelman, and N. Mandahl. 2010. Generation of trisomies in cancer cells by multipolar mitosis and incomplete cytokinesis. *Proc Natl Acad Sci U S A*. 107:20489-20493.

Haschka, M., G. Karbon, L.L. Fava, and A. Villunger. 2018. Perturbing mitosis for anti‐cancer therapy: is cell death the only answer? *EMBO reports*. 19:e45440.

Horiuchi, M., T. Kuga, Y. Saito, M. Nagano, J. Adachi, T. Tomonaga, N. Yamaguchi, and Y. Nakayama. 2018. The tyrosine kinase v-Src causes mitotic slippage by phosphorylating an inhibitory tyrosine residue of Cdk1. *J Biol Chem*. 293:15524-15537.

Hsu, S.H., E.R. Delgado, P.A. Otero, K.Y. Teng, H. Kutay, K.M. Meehan, J.B. Moroney, J.K. Monga, N.J. Hand, J.R. Friedman, K. Ghoshal, and A.W. Duncan. 2016. MicroRNA-122 regulates polyploidization in the murine liver. *Hepatology*. 64:599-615.

Kuznetsova, A.Y., K. Seget, G.K. Moeller, M.S. de Pagter, J.A.D.M. de Roos, M. Dürrbaum, C. Kuffer, S. Müller, G.J.R. Zaman, W.P. Kloosterman, and Z. Storchová. 2015. Chromosomal instability, tolerance of mitotic errors and multidrug resistance are promoted by tetraploidization in human cells. *Cell Cycle*. 14:2810-2820.

Kwon, M., S.A. Godinho, N.S. Chandhok, N.J. Ganem, A. Azioune, M. Thery, and D. Pellman. 2008. Mechanisms to suppress multipolar divisions in cancer cells with extra centrosomes. *Genes Dev*. 22:2189-2203.

Lau, T.Y., and R.Y.C. Poon. 2023. Whole-Genome Duplication and Genome Instability in Cancer Cells: Double the Trouble. *Int J Mol Sci*. 24.

Ma, H., A. Naseri, P. Reyes-Gutierrez, S.A. Wolfe, S. Zhang, and T. Pederson. 2015. Multicolor CRISPR labeling of chromosomal loci in human cells. *Proceedings of the National Academy of Sciences*. 112:3002-3007.

Mazzi, S., L. Lordier, N. Debili, H. Raslova, and W. Vainchenker. 2018. Megakaryocyte and polyploidization. *Experimental Hematology*. 57:1-13.

McKinney, S.A., C.S. Murphy, K.L. Hazelwood, M.W. Davidson, and L.L. Looger. 2009. A bright and

1187 photostable photoconvertible fluorescent protein. *Nat Methods*. 6:131-133.
1188 Mondal, G., S. Sengupta, C.K. Panda, S.M. Gollin, W.S. Saunders, and S. Roychoudhury. 2007.
1189 Overexpression of Cdc20 leads to impairment of the spindle assembly checkpoint and
1190 aneuploidization in oral cancer. *Carcinogenesis*. 28:81-92.
1191 Nelles, D.A., M.Y. Fang, M.R. O'Connell, J.L. Xu, S.J. Markmiller, J.A. Doudna, and G.W. Yeo. 2016.
1192 Programmable RNA Tracking in Live Cells with CRISPR/Cas9. *Cell*. 165:488-496.
1193 Piehl, M., and L. Cassimeris. 2003. Organization and dynamics of growing microtubule plus ends during
1194 early mitosis. *Mol Biol Cell*. 14:916-925.
1195 Potapova, T.A., C.W. Seidel, A.C. Box, G. Rancati, and R. Li. 2016. Transcriptome analysis of
1196 tetraploid cells identifies cyclin D2 as a facilitator of adaptation to genome doubling in
1197 the presence of p53. *Mol Biol Cell*. 27:3065-3084.
1198 Ran, F.A., P.D. Hsu, J. Wright, V. Agarwala, D.A. Scott, and F. Zhang. 2013. Genome engineering using
1199 the CRISPR-Cas9 system. *Nat Protoc*. 8:2281-2308.
1200 Rankin, S., N.G. Ayad, and M.W. Kirschner. 2005. Sororin, a Substrate of the Anaphase- Promoting
1201 Complex, Is Required for Sister Chromatid Cohesion in Vertebrates. *Molecular Cell*. 18:185-200.
1202 Rios, A.C., N.Y. Fu, P.R. Jamieson, B. Pal, L. Whitehead, K.R. Nicholas, G.J. Lindeman, and J.E.
1203 Visvader. 2016. Essential role for a novel population of binucleated mammary epithelial cells
1204 in lactation. *Nat Commun*. 7:11400.
1205 Sakurikar, N., J.M. Eichhorn, and T.C. Chambers. 2012. Cyclin-dependent kinase-1 (Cdk1)/cyclin B1
1206 dictates cell fate after mitotic arrest via phosphoregulation of antiapoptotic Bcl-2 proteins.
1207 *J Biol Chem*. 287:39193-39204.
1208 Sanz-Gómez, N., I. de Pedro, B. Ortigosa, D. Santamaría, M. Malumbres, G. de Cárcer, and A. Gandarillas.
1209 2020. Squamous differentiation requires G2/mitosis slippage to avoid apoptosis. *Cell Death*
1210 *Differ*. 27:2451-2467.
1211 Sanz-Gómez, N., M. González-Álvarez, J. De Las Rivas, and G. de Cárcer. 2023. Whole-Genome Doubling
1212 as a source of cancer: how, when, where, and why? *Front Cell Dev Biol*. 11:1209136.
1213 Schmitz, J., E. Watrin, P. Lénárt, K. Mechtler, and J.-M. Peters. 2007. Sororin Is Required for Stable
1214 Binding of Cohesin to Chromatin and for Sister Chromatid Cohesion in Interphase. *Current*
1215 *Biology*. 17:630-636.
1216 Schnerch, D., A. Schmidts, M. Follo, J. Udi, J. Felthaus, D. Pfeifer, M. Engelhardt, and R. Wäsch.
1217 2013. BubR1 is frequently repressed in acute myeloid leukemia and its re-expression sensitizes
1218 cells to antimitotic therapy. *Haematologica*. 98:1886-1895.
1219 Silkworth, W.T., I.K. Nardi, L.M. Scholl, and D. Cimini. 2009. Multipolar spindle pole coalescence
1220 is a major source of kinetochore mis-attachment and chromosome mis-segregation in cancer cells.
1221 *PLoS One*. 4:e6564.
1222 Soeda, S., Y. Nakayama, T. Honda, A. Aoki, N. Tamura, K. Abe, Y. Fukumoto, and N. Yamaguchi. 2013.
1223 v-Src causes delocalization of Mklp1, Aurora B, and INCENP from the spindle midzone during
1224 cytokinesis failure. *Exp Cell Res*. 319:1382-1397.
1225 Soonpaa, M.H., K.K. Kim, L. Pajak, M. Franklin, and L.J. Field. 1996. Cardiomyocyte DNA synthesis

1226 and binucleation during murine development. *Am J Physiol*. 271:H2183-2189.
1227 Sze, K.M.-F., Y.-P. Ching, D.-Y. Jin, and I. Oi-Lin Ng. 2004. Association of MAD2 expression with
1228 mitotic checkpoint competence in hepatoma cells. *Journal of Biomedical Science*. 11:920-927.
1229 Van de Peer, Y., E. Mizrachi, and K. Marchal. 2017. The evolutionary significance of polyploidy. *Nature*
1230 *Reviews Genetics*. 18:411-424.
1231 van Rijnberk, L.M., R. Barrull-Mascaró, R.L. van der Palen, E.S. Schild, H.C. Korswagen, and M. Galli.
1232 2022. Endomitosis controls tissue-specific gene expression during development. *PLOS Biology*.
1233 20:e3001597.
1234 Wang, X., D.Y. Jin, R.W. Ng, H. Feng, Y.C. Wong, A.L. Cheung, and S.W. Tsao. 2002. Significance of
1235 MAD2 expression to mitotic checkpoint control in ovarian cancer cells. *Cancer Res*.
1236 62:1662-1668.
1237 Was, H., A. Borkowska, A. Olszewska, A. Klemba, M. Marciniak, A. Synowiec, and C. Kieda. 2022.
1238 Polyploidy formation in cancer cells: How a Trojan horse is born. *Seminars in Cancer Biology*.
1239 81:24-36.
1240 Yang, C., X. Shi, Y. Huang, Z. Zhang, H.J. Cooke, M. Wang, and Q. Shi. 2012. Rapid proliferation of
1241 daughter cells lacking particular chromosomes due to multipolar mitosis promotes clonal
1242 evolution in colorectal cancer cells. *Cell Cycle*. 11:2650-2659.
1243 Yesbolatova, A., Y. Saito, N. Kitamoto, H. Makino-Itou, R. Ajima, R. Nakano, H. Nakaoka, K. Fukui,
1244 K. Gamo, Y. Tominari, H. Takeuchi, Y. Saga, K.I. Hayashi, and M.T. Kanemaki. 2020. The
1245 auxin-inducible degron 2 technology provides sharp degradation control in yeast, mammalian
1246 cells, and mice. *Nat Commun*. 11:5701.
1247

Figure 1

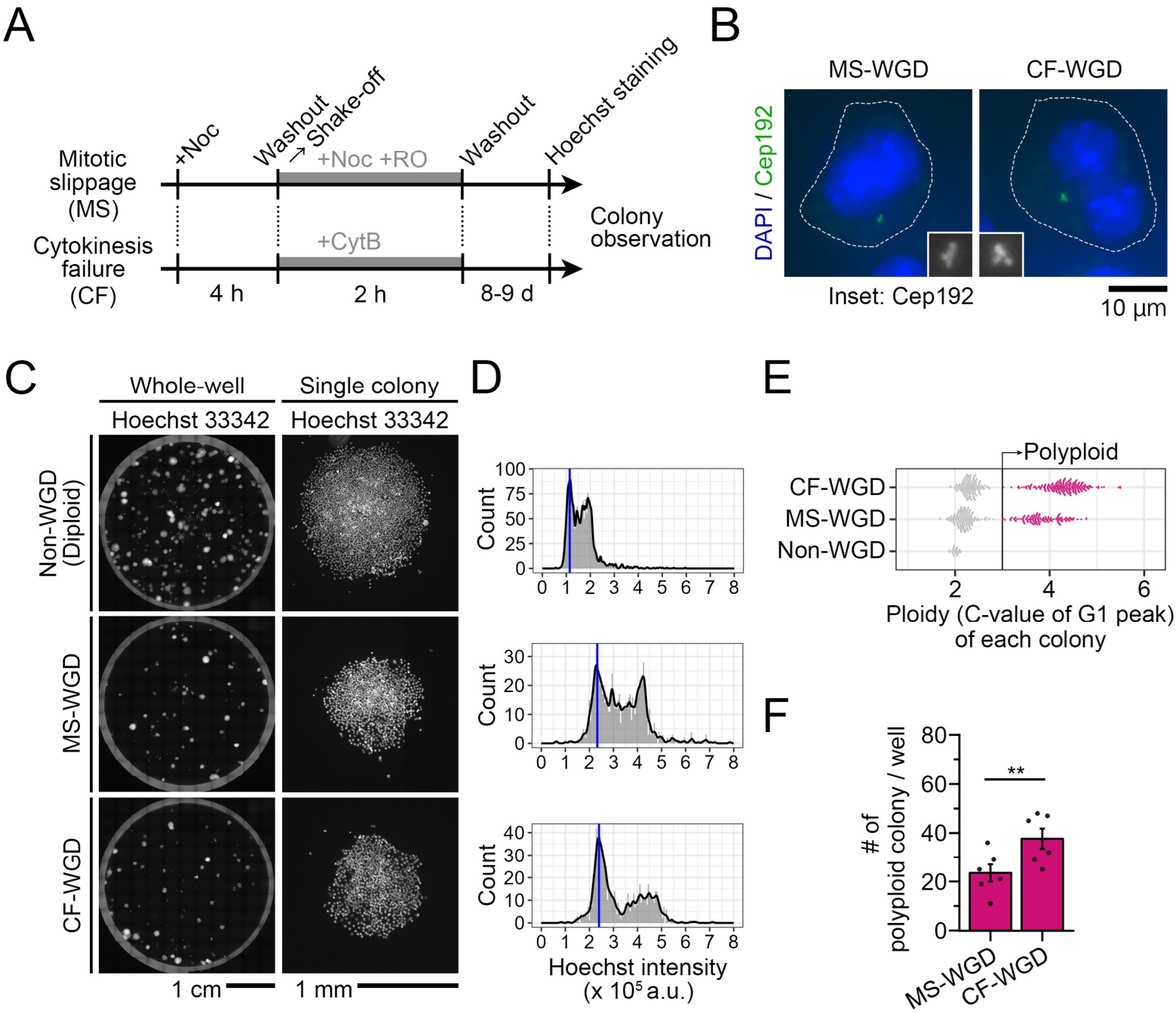
A
Mitotic slippage (MS)
Cytokinesis failure (CF)
+Noc
Washout → Shake-off
+Noc +RO
Washout
Hoechst staining
+CytB
Colony observation
4 h
2 h
8-9 d
B
MS-WGD
CF-WGD
DAPI / Cep192
Inset: Cep192
10 µm
C
Whole-well
Single colony
Hoechst 33342
Hoechst 33342
Non-WGD (Diploid)
MS-WGD
CF-WGD
1 cm
1 mm
D
Count
Hoechst intensity (x 10^5 a.u.)
E
Polyploid
CF-WGD
MS-WGD
Non-WGD
Ploidy (C-value of G1 peak) of each colony
F
# of polyploid colony / well
**
MS-WGD
CF-WGD

Figure 2

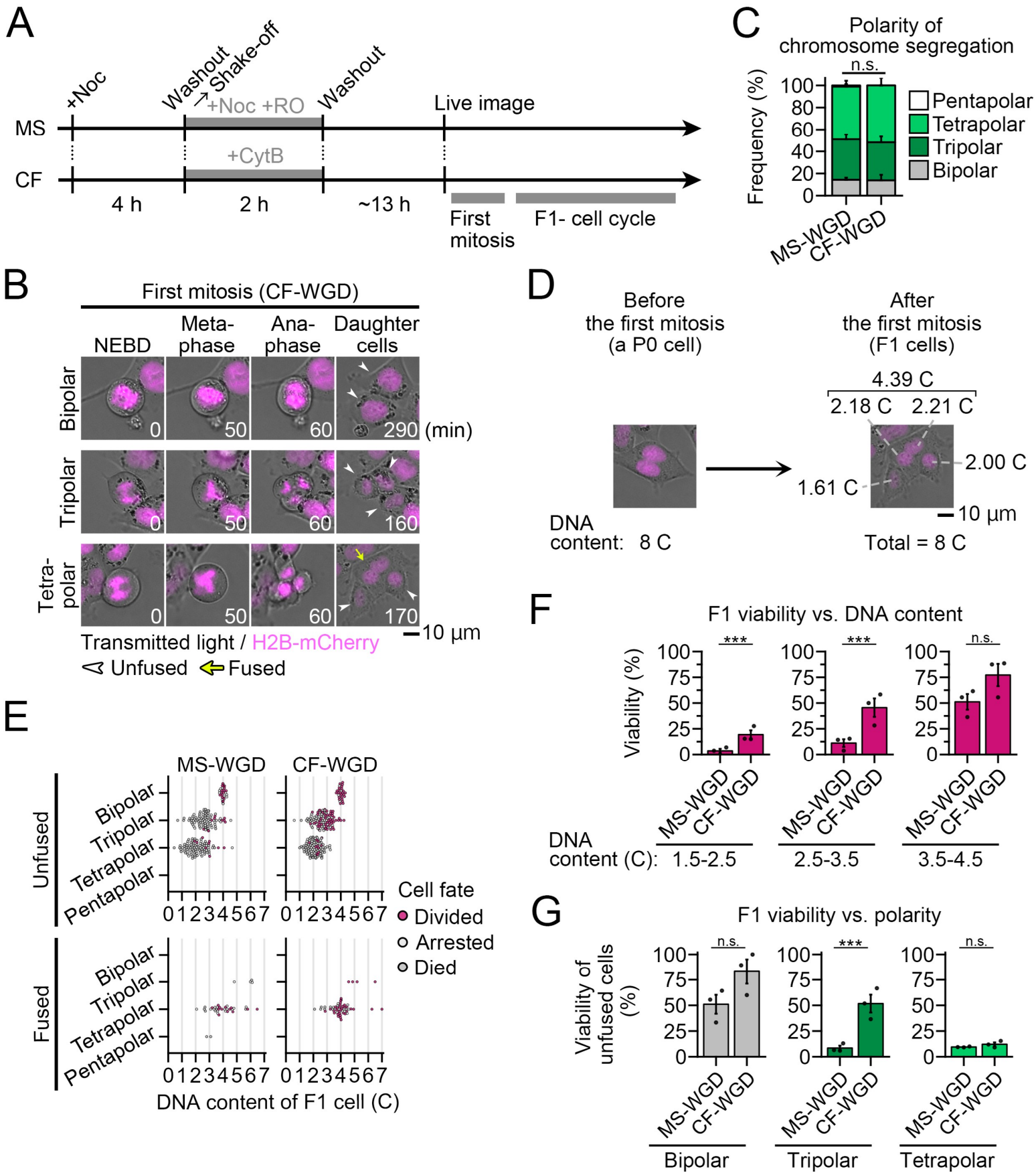
A
+Noc
Washout
Shake-off
+Noc +RO
Washout
Live image
MS
+CytB
CF
4 h
2 h
~13 h
First mitosis
F1- cell cycle
B
First mitosis (CF-WGD)
NEBD
Meta-phase
Ana-phase
Daughter cells
Bipolar
Tripolar
Tetra-polar
0
50
60
290
160
170
(min)
10 µm
Transmitted light / H2B-mCherry
Unfused
Fused
C
Polarity of chromosome segregation
n.s.
Frequency (%)
100
80
60
40
20
0
Pentapolar
Tetrapolar
Tripolar
Bipolar
MS-WGD
CF-WGD
D
Before the first mitosis (a P0 cell)
After the first mitosis (F1 cells)
4.39 C
2.18 C
2.21 C
2.00 C
1.61 C
10 µm
DNA content: 8 C
Total = 8 C
E
MS-WGD
CF-WGD
Unfused
Fused
Bipolar
Tripolar
Tetrapolar
Pentapolar
0 1 2 3 4 5 6 7
Cell fate
Divided
Arrested
Died
DNA content of F1 cell (C)
F
F1 viability vs. DNA content
***
n.s.
Viability (%)
100
75
50
25
0
MS-WGD
CF-WGD
DNA content (C):
1.5-2.5
2.5-3.5
3.5-4.5
G
F1 viability vs. polarity
Viability of unfused cells (%)
Bipolar
Tripolar
Tetrapolar

Figure 3

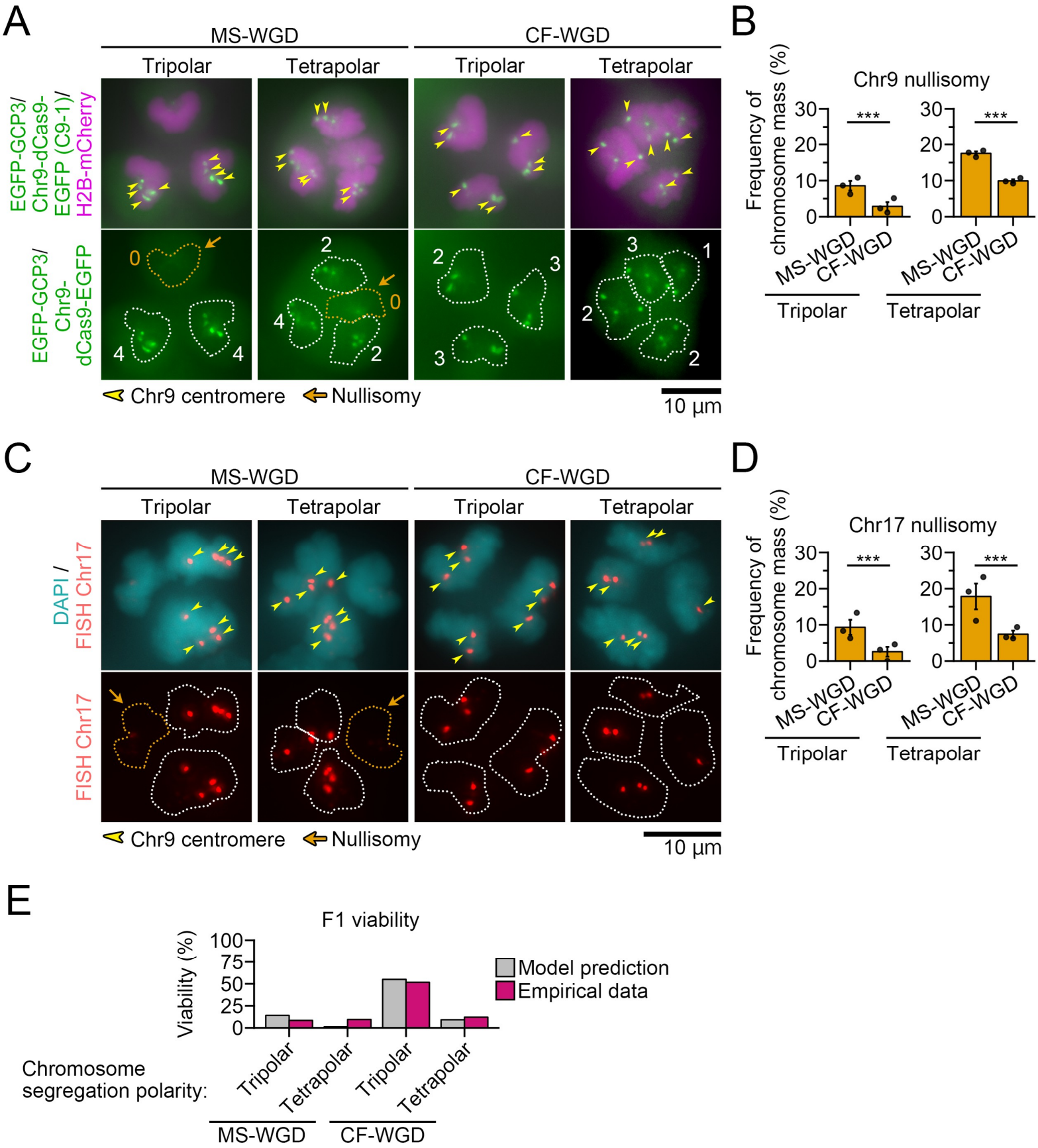
A
MS-WGD
CF-WGD
Tripolar
Tetrapolar
Tripolar
Tetrapolar
EGFP-GCP3/
Chr9-dCas9-
EGFP (C9-1)/
H2B-mCherry
EGFP-GCP3/
Chr9-
dCas9-EGFP
Chr9 centromere
Nullisomy
10 µm
B
Chr9 nullisomy
Frequency of chromosome mass (%)
***
MS-WGD
CF-WGD
Tripolar
Tetrapolar
C
DAPI /
FISH Chr17
FISH Chr17
Chr9 centromere
Nullisomy
10 µm
D
Chr17 nullisomy
Frequency of chromosome mass (%)
***
MS-WGD
CF-WGD
Tripolar
Tetrapolar
E
F1 viability
Viability (%)
Model prediction
Empirical data
Chromosome segregation polarity:
Tripolar
Tetrapolar
Tripolar
Tetrapolar
MS-WGD
CF-WGD

Figure 4

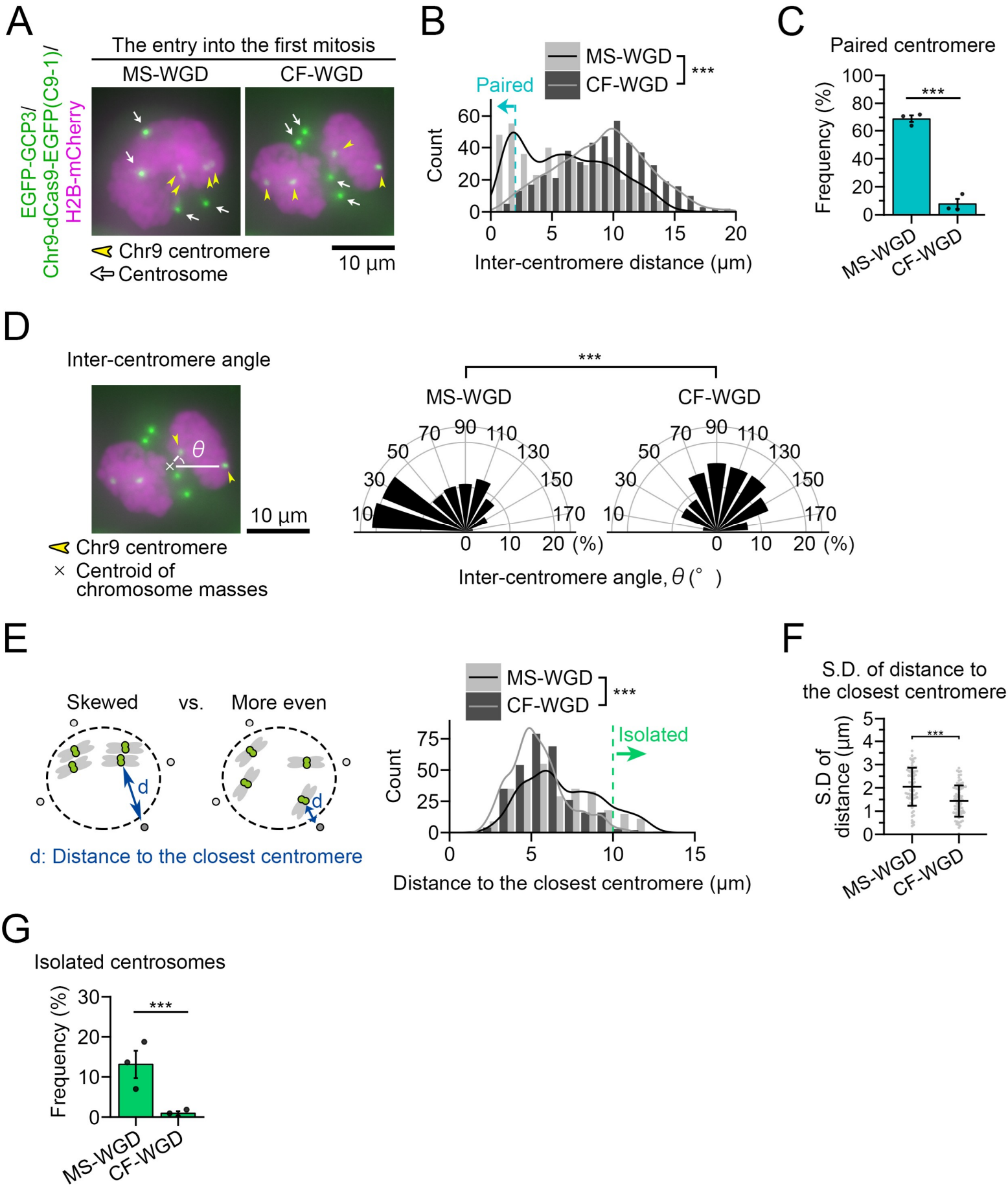
A
The entry into the first mitosis
MS-WGD
CF-WGD
EGFP-GCP3/
Chr9-dCas9-EGFP(C9-1)/
H2B-mCherry
Chr9 centromere
Centrosome
10 μm
B
MS-WGD
CF-WGD
***
Paired
Count
Inter-centromere distance (μm)
C
Paired centromere
Frequency (%)
***
MS-WGD
CF-WGD
D
Inter-centromere angle
θ
10 μm
Chr9 centromere
Centroid of chromosome masses
***
MS-WGD
CF-WGD
(%)
Inter-centromere angle, θ (°)
E
Skewed
vs.
More even
d
d: Distance to the closest centromere
MS-WGD
CF-WGD
***
Isolated
Count
Distance to the closest centromere (μm)
F
S.D. of distance to the closest centromere
S.D of distance (μm)
***
MS-WGD
CF-WGD
G
Isolated centrosomes
Frequency (%)
***
MS-WGD
CF-WGD

Figure 5

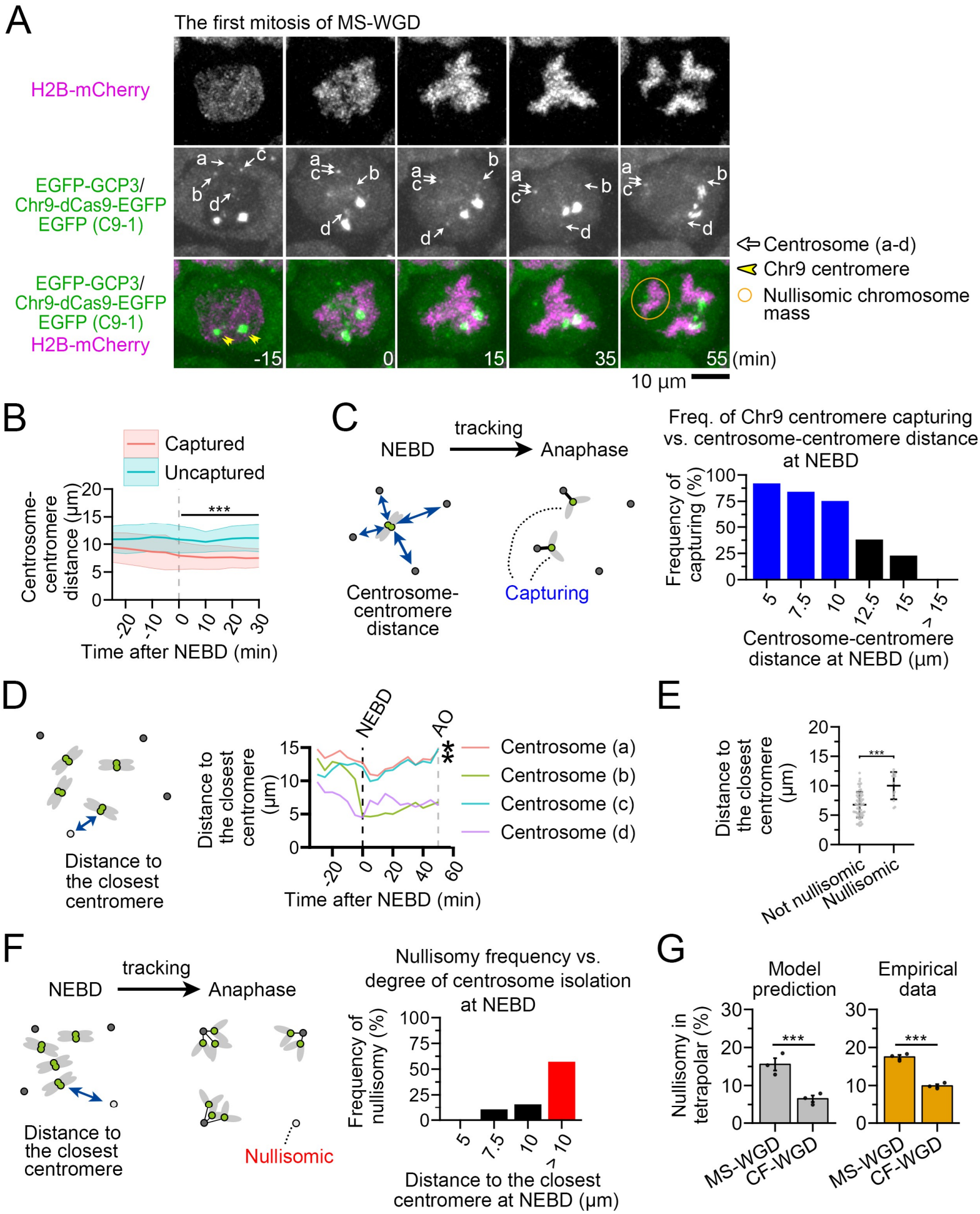
A
The first mitosis of MS-WGD
H2B-mCherry
EGFP-GCP3/
Chr9-dCas9-EGFP
EGFP (C9-1)
EGFP-GCP3/
Chr9-dCas9-EGFP
EGFP (C9-1)
H2B-mCherry
-15
0
15
35
55 (min)
10 µm
Centrosome (a-d)
Chr9 centromere
Nullisomic chromosome mass
B
Captured
Uncaptured
Centrosome-centromere distance (µm)
***
Time after NEBD (min)
C
NEBD
tracking
Anaphase
Centrosome-centromere distance
Capturing
Freq. of Chr9 centromere capturing vs. centrosome-centromere distance at NEBD
Frequency of capturing (%)
Centrosome-centromere distance at NEBD (µm)
D
Distance to the closest centromere
NEBD
AO
**
Distance to the closest centromere (µm)
Centrosome (a)
Centrosome (b)
Centrosome (c)
Centrosome (d)
Time after NEBD (min)
E
Distance to the closest centromere (µm)
***
Not nullisomic
Nullisomic
F
NEBD
tracking
Anaphase
Distance to the closest centromere
Nullisomic
Nullisomy frequency vs. degree of centrosome isolation at NEBD
Frequency of nullisomy (%)
Distance to the closest centromere at NEBD (µm)
G
Model prediction
Empirical data
Nullisomy in tetrapolar (%)
***
MS-WGD
CF-WGD

Figure 6

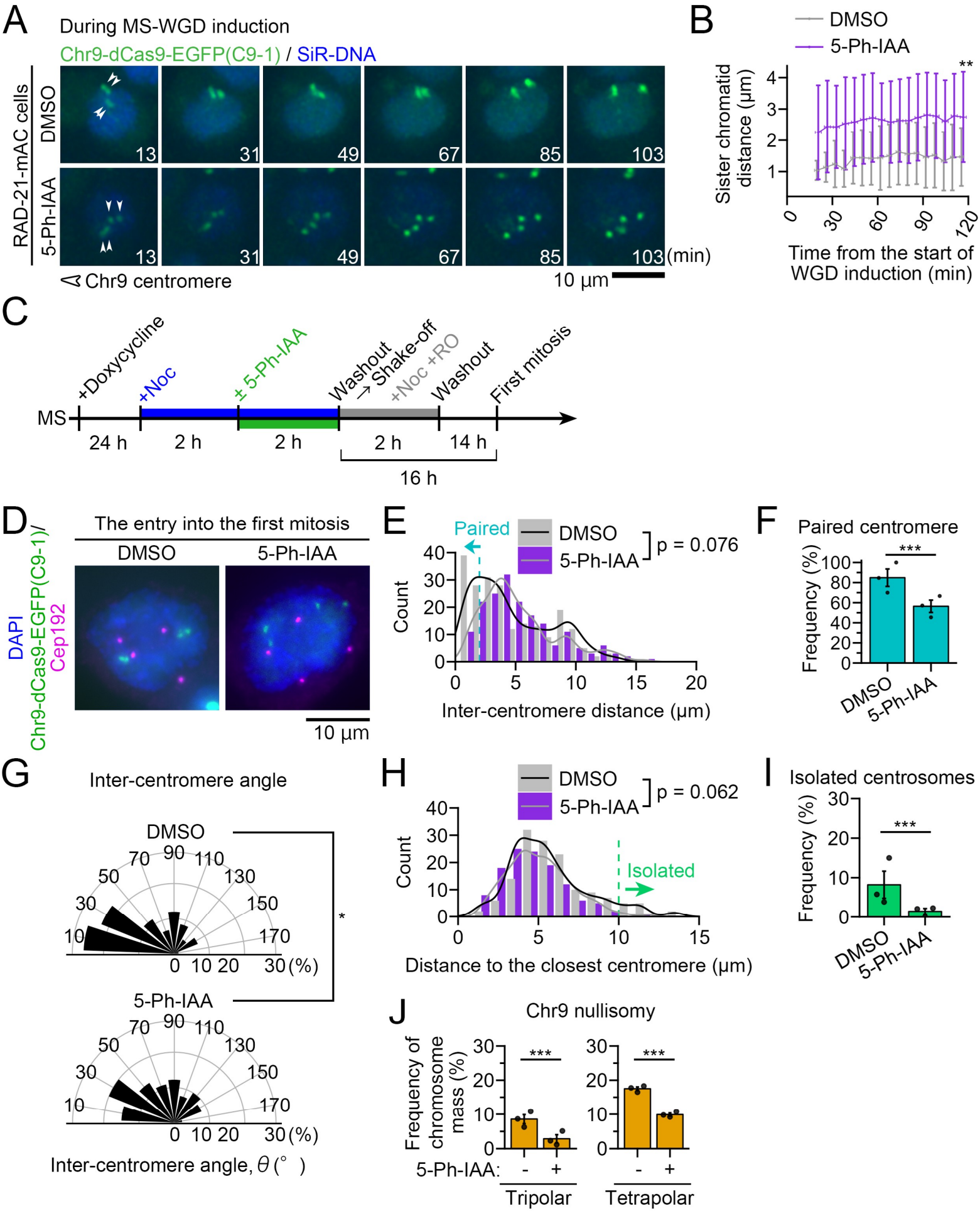
A
During MS-WGD induction
Chr9-dCas9-EGFP(C9-1) / SiR-DNA
RAD-21-mAC cells
DMSO
5-Ph-IAA
13
31
49
67
85
103
(min)
Chr9 centromere
10 µm
B
DMSO
5-Ph-IAA
Sister chromatid distance (µm)
Time from the start of WGD induction (min)
C
+Doxycycline
+Noc
± 5-Ph-IAA
Washout → Shake-off
+Noc +RO
Washout
First mitosis
MS
24 h
2 h
2 h
2 h
14 h
16 h
D
The entry into the first mitosis
DMSO
5-Ph-IAA
DAPI
Chr9-dCas9-EGFP(C9-1)/
Cep192
10 µm
E
Paired
DMSO
5-Ph-IAA
p = 0.076
Count
Inter-centromere distance (µm)
F
Paired centromere
Frequency (%)
DMSO
5-Ph-IAA
G
Inter-centromere angle
DMSO
5-Ph-IAA
(%)
Inter-centromere angle, θ (°)
H
DMSO
5-Ph-IAA
p = 0.062
Isolated
Count
Distance to the closest centromere (µm)
I
Isolated centrosomes
Frequency (%)
DMSO
5-Ph-IAA
J
Chr9 nullisomy
Frequency of chromosome mass (%)
5-Ph-IAA:
Tripolar
Tetrapolar

Figure 7

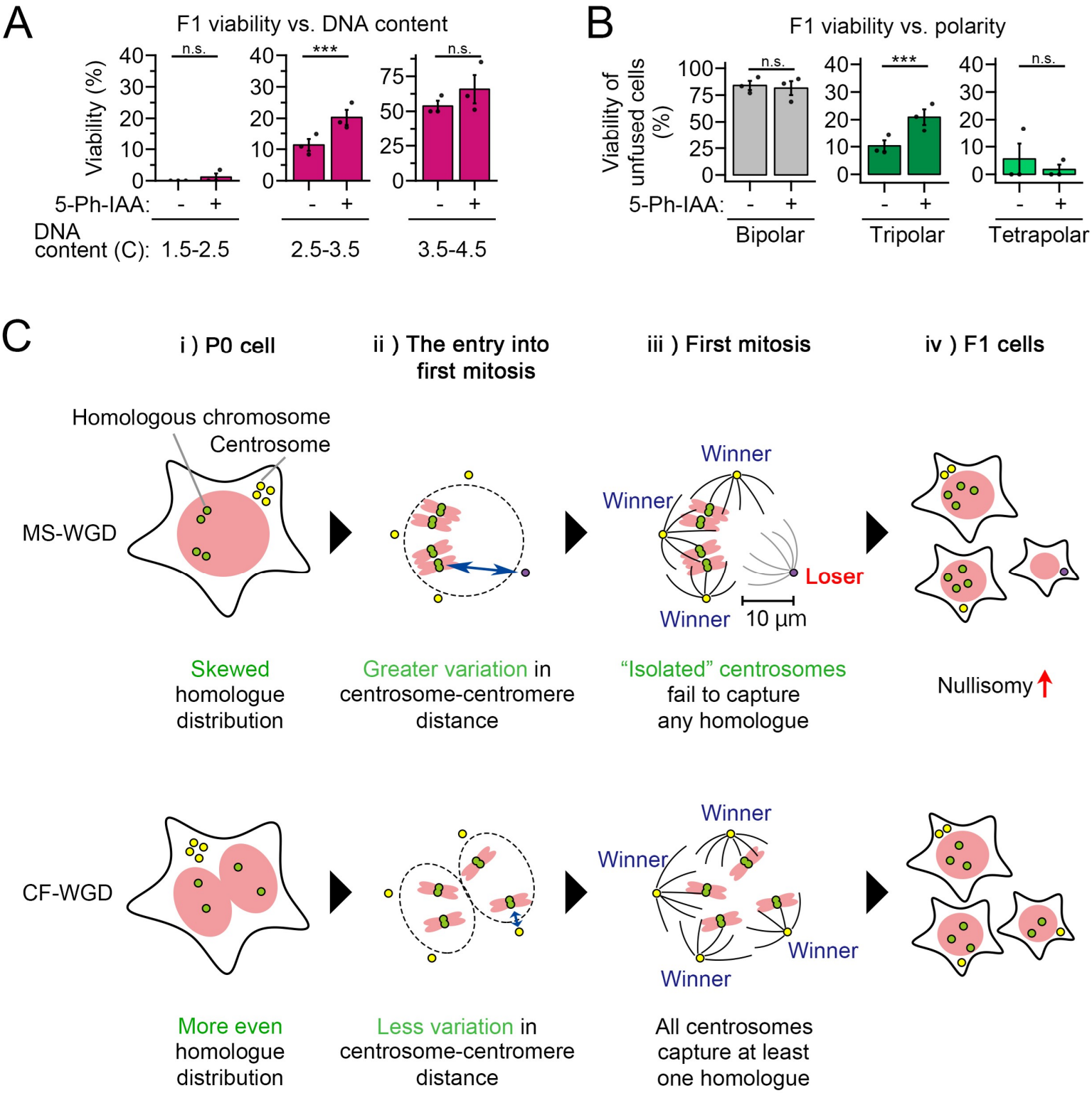
A
F1 viability vs. DNA content
Viability (%)
n.s.
***
n.s.
5-Ph-IAA: - +
DNA content (C): 1.5-2.5
2.5-3.5
3.5-4.5
B
F1 viability vs. polarity
Viability of unfused cells (%)
n.s.
***
n.s.
5-Ph-IAA: - +
Bipolar
Tripolar
Tetrapolar
C
i) P0 cell
ii) The entry into first mitosis
iii) First mitosis
iv) F1 cells
Homologous chromosome
Centrosome
MS-WGD
Winner
Winner
Loser
Winner
10 µm
Skewed homologue distribution
Greater variation in centrosome-centromere distance
"Isolated" centrosomes fail to capture any homologue
Nullisomy
CF-WGD
Winner
Winner
Winner
Winner
More even homologue distribution
Less variation in centrosome-centromere distance
All centrosomes capture at least one homologue

Supplementaly figure 1

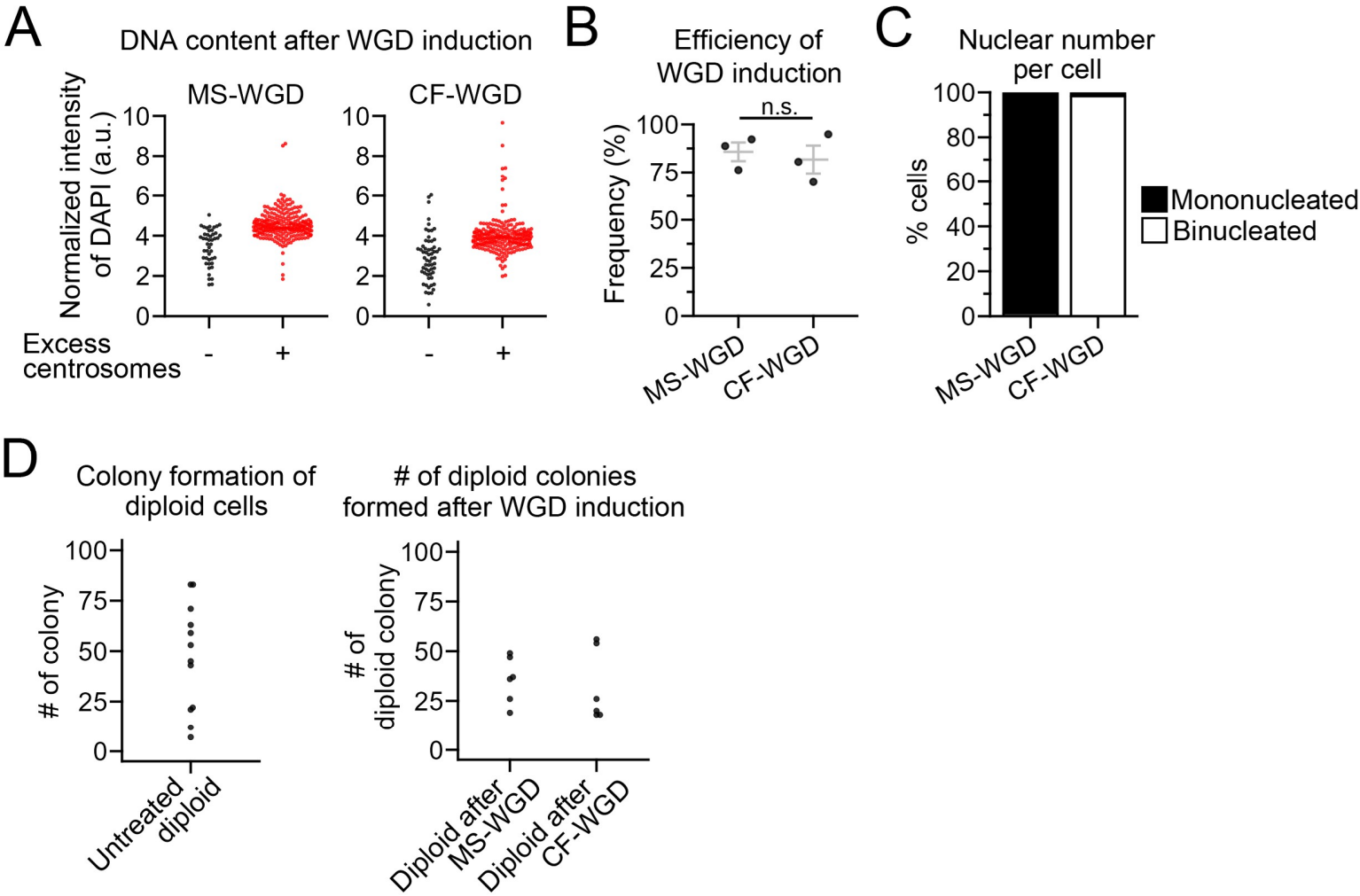

Supplementaly figure 2

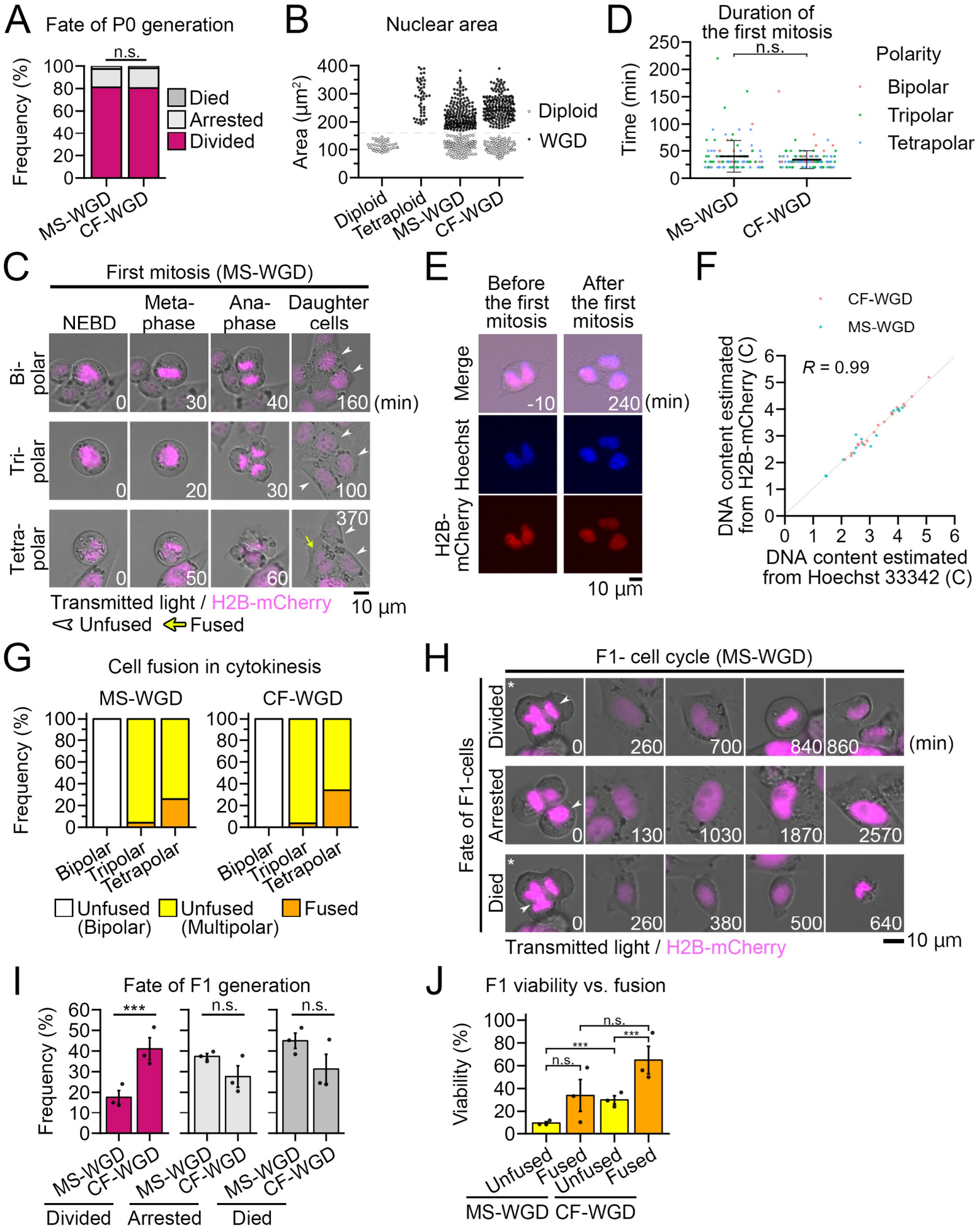

Supplementaly figure 3

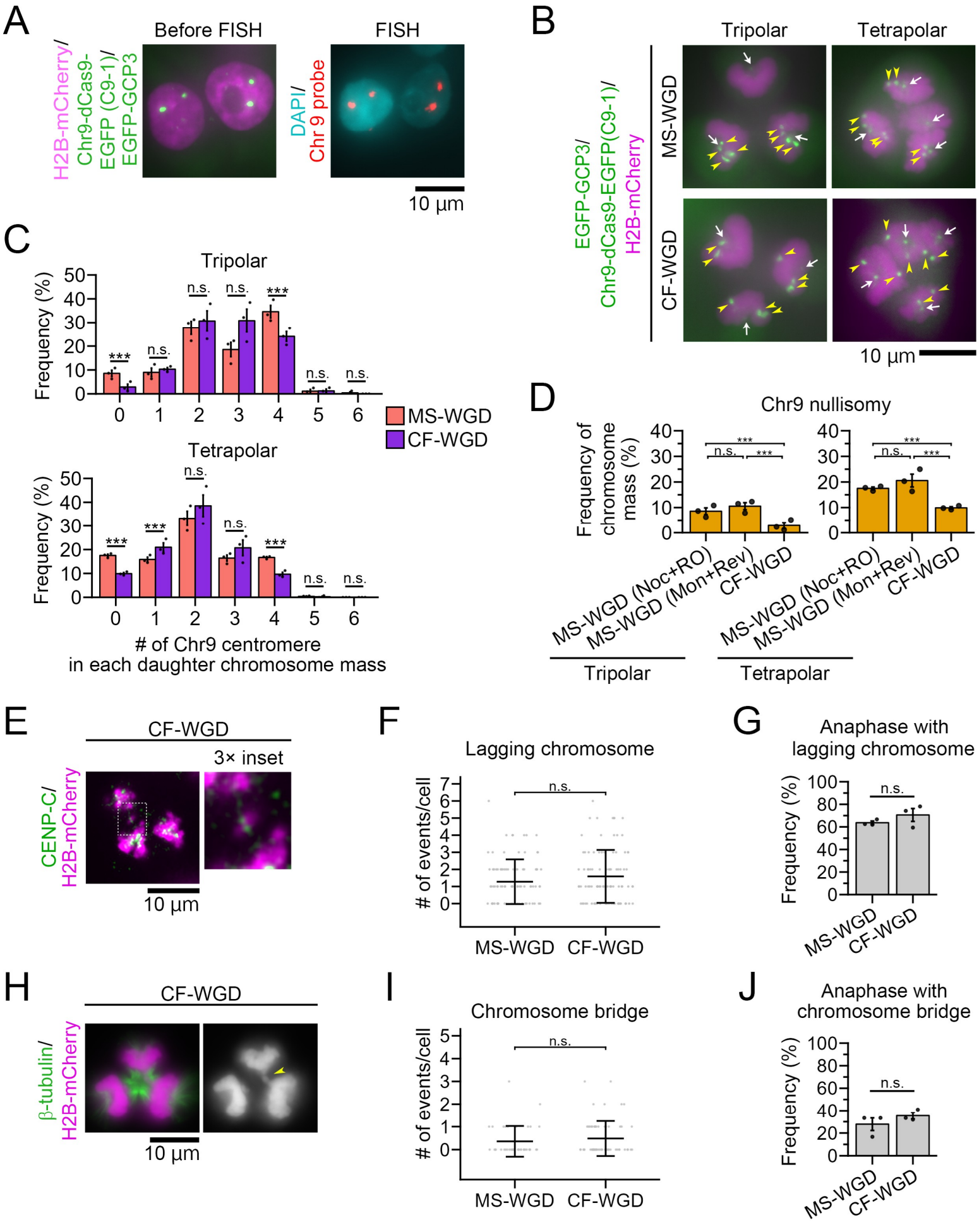

Supplementaly figure 4

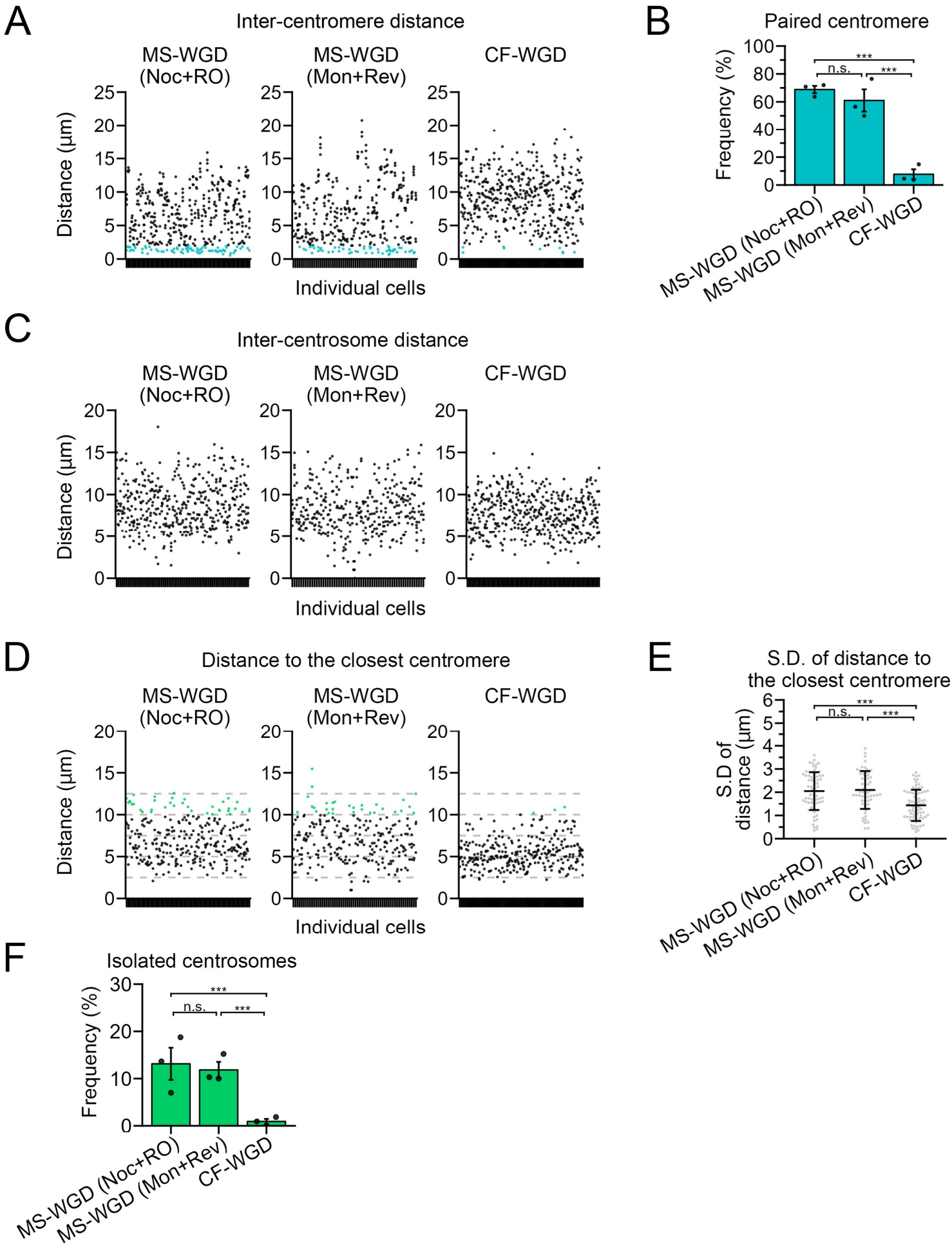

Supplementaly figure 5

A

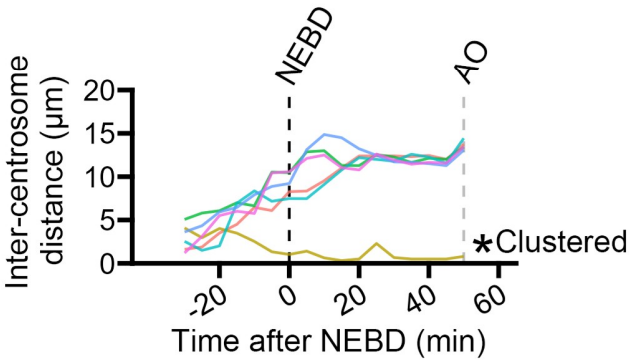

B

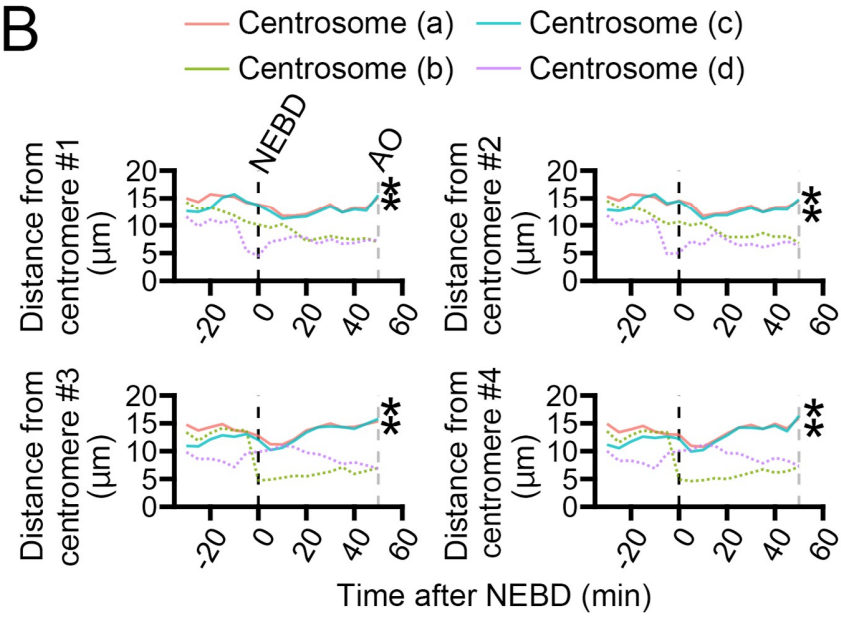

C

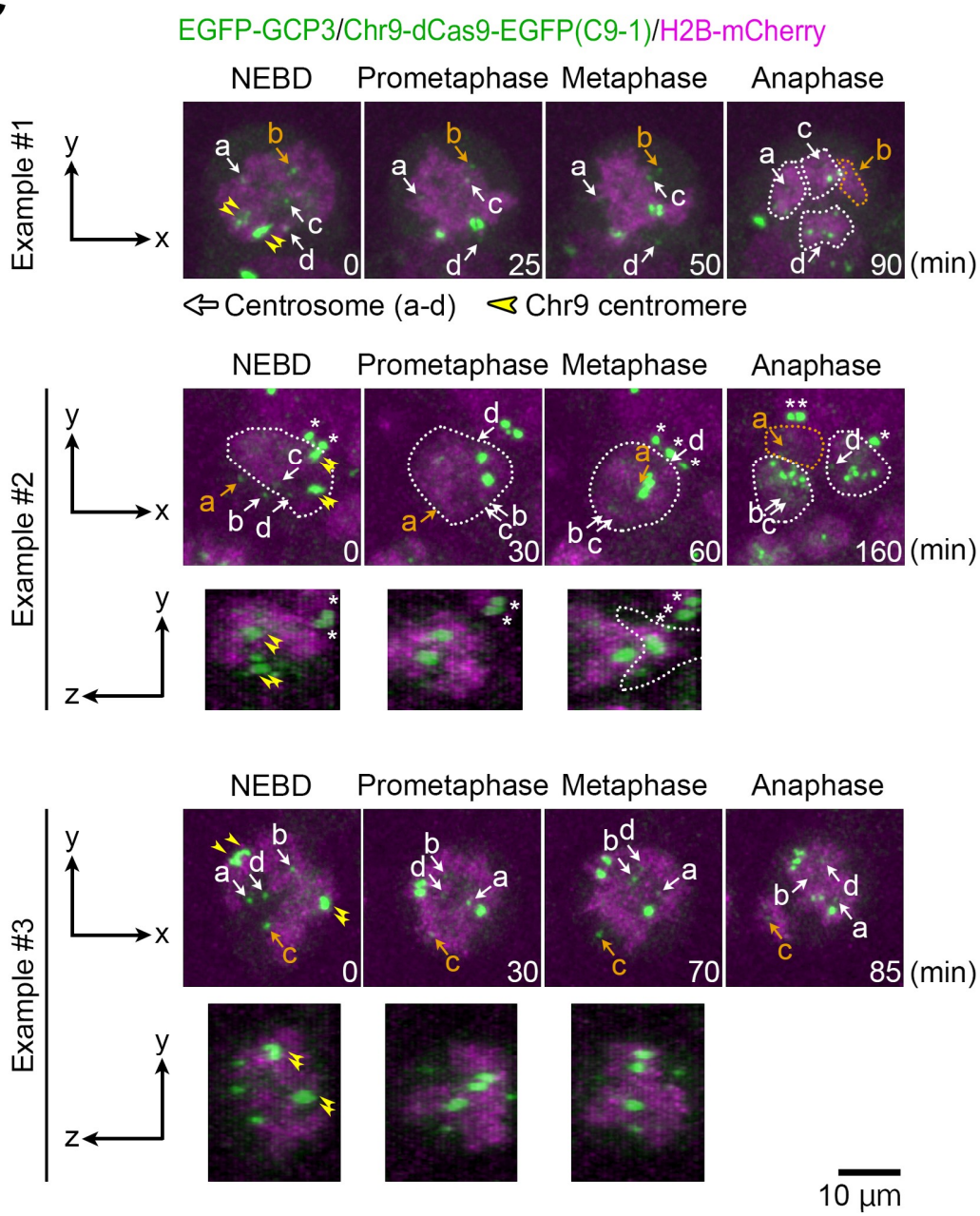

Supplementaly figure 6

A

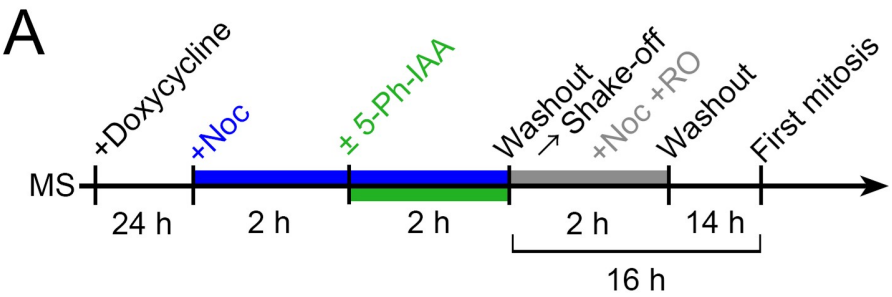

B

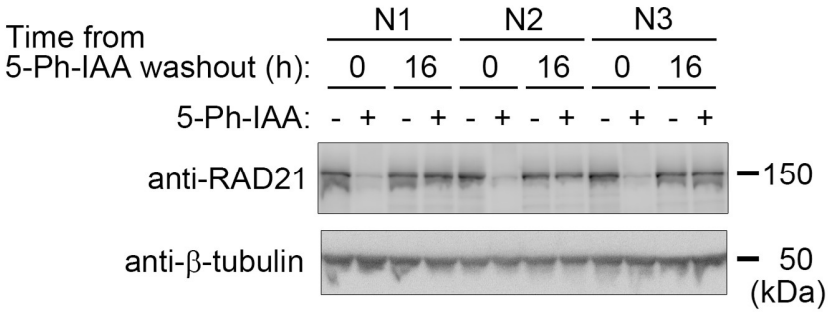

C

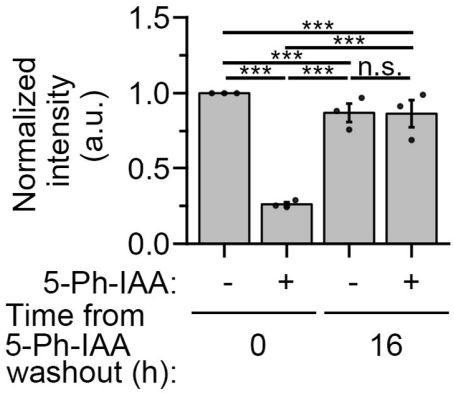

D

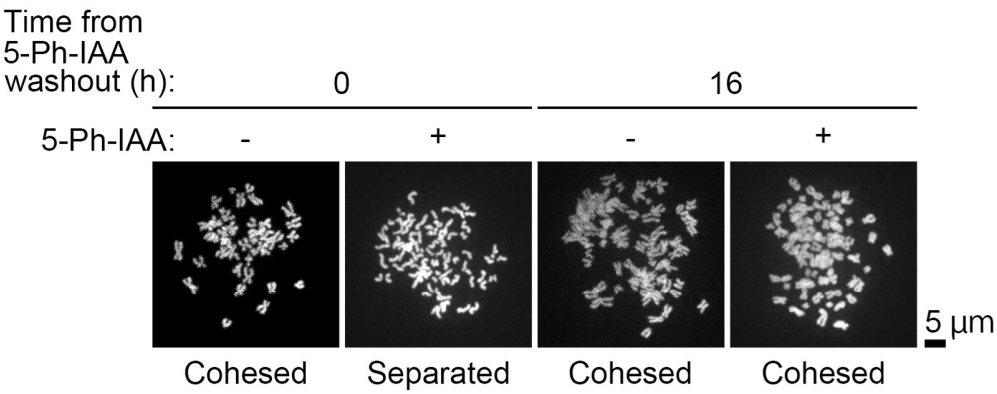

E

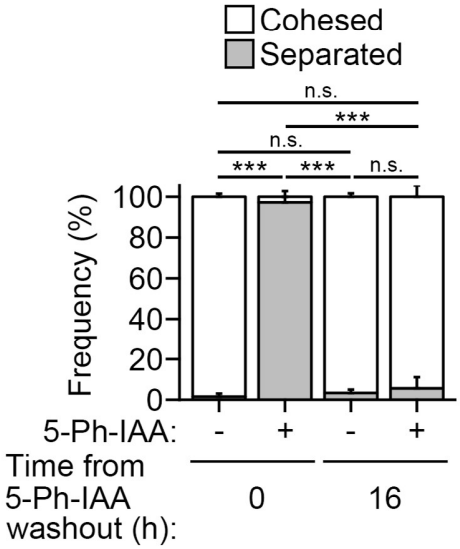

Supplementaly figure 7

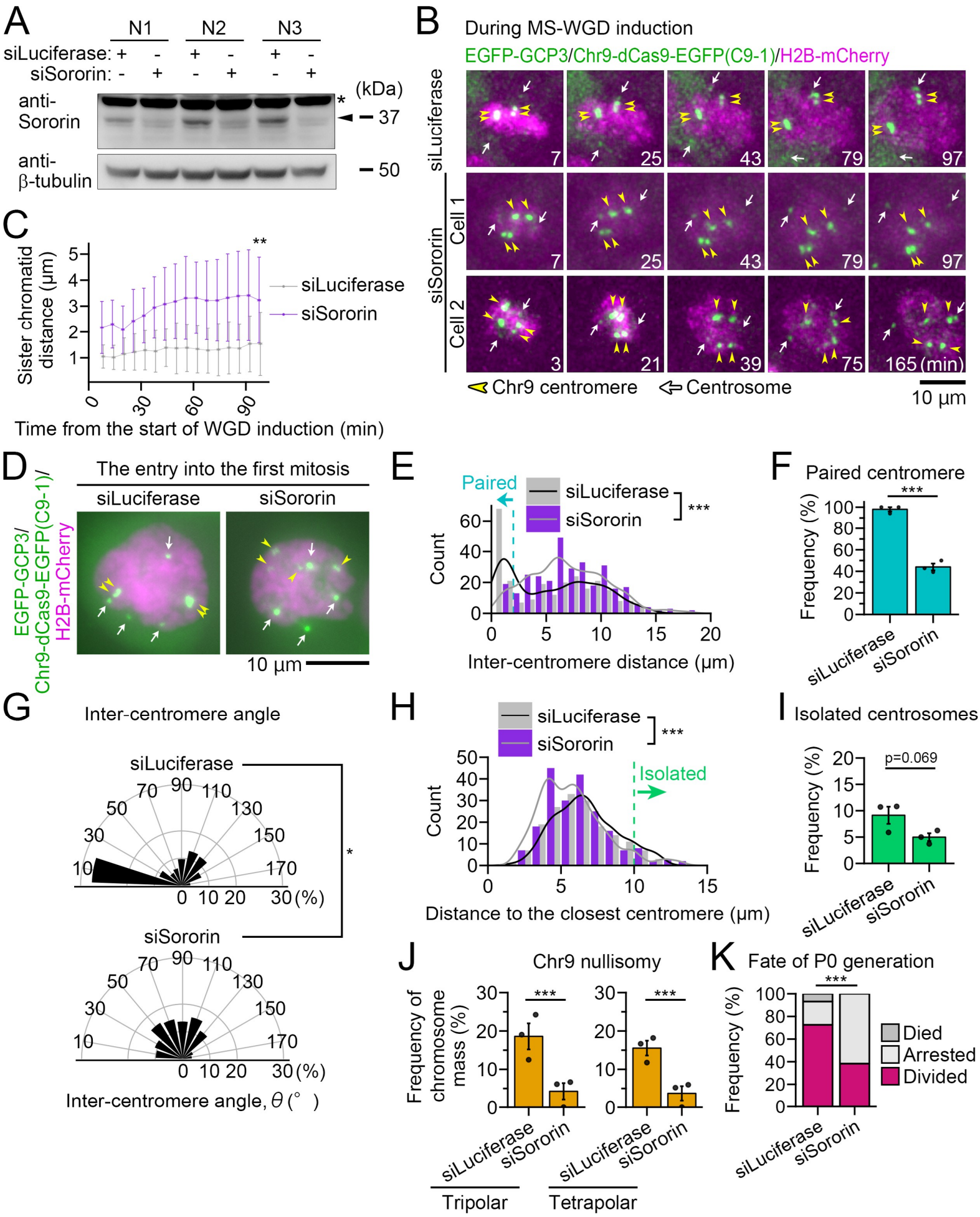

Supplementaly figure 8

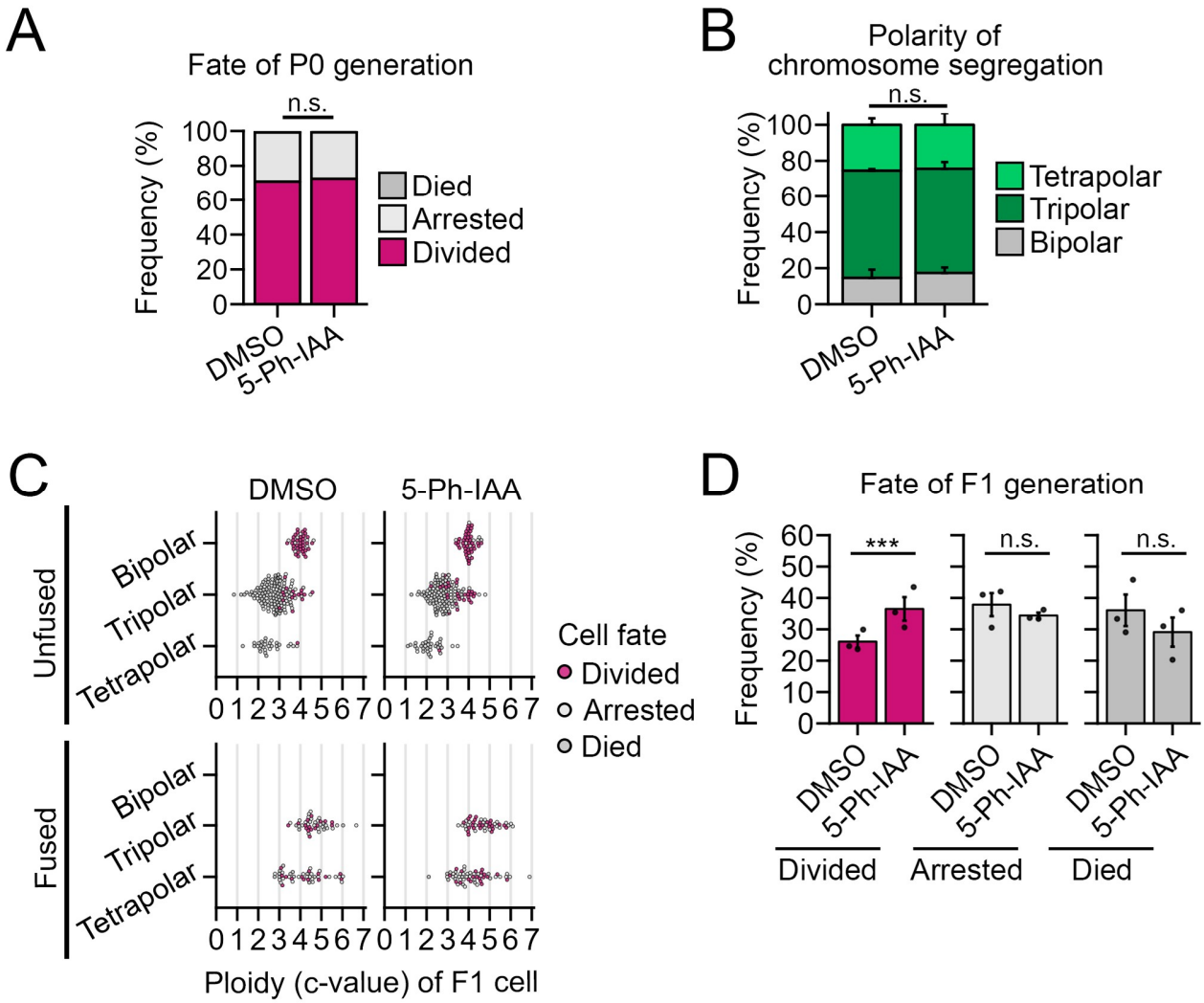

Supplementaly figure 9

Figure 7B

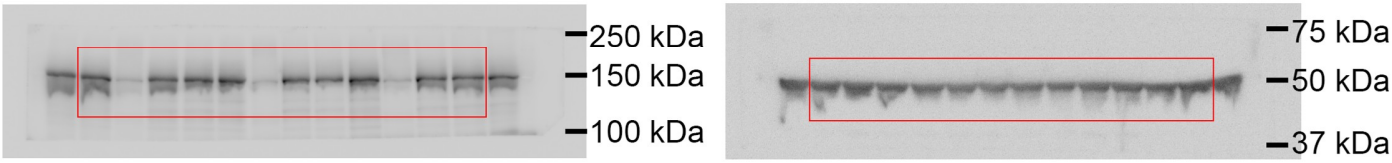
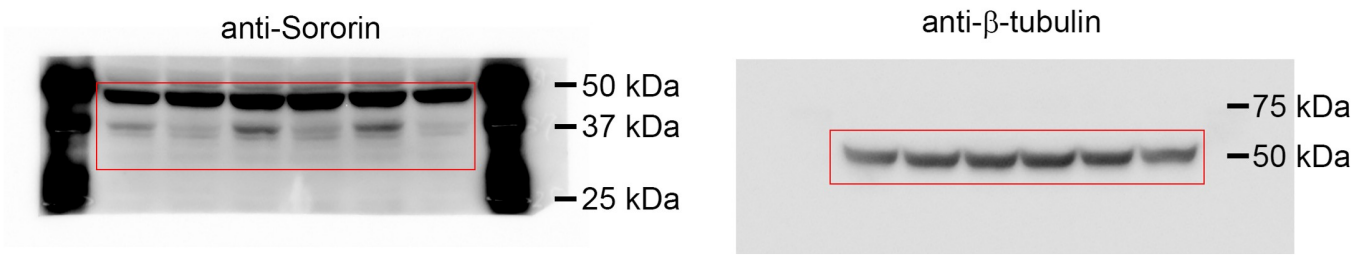
Supplementaly figure 6A